Study of Glucose sensor's sensitivity and impedance over time and an embedded system for their real-time measurement

Xiaotian Zhang

A Thesis submitted in fulfilment of requirements for the degree of
Master of Science
Analogue and Digital Integrated Circuit Design
of Imperial College London

Department of Electrical and Electronic Engineering
Imperial College London
September 7, 2016

Abstract

THE thesis aims to study the sensitivity as well as the impedance of the glucose sensor over certain period of time, in order to develop a new algorithm to predict the sensor performance without performing a time-consuming chronoamperometry measurement. Specifically, this research studies the correlation of the sensor's impedance with its sensitivity over time. Sensitivity m of sensor seems to be related to both double-layer capacitance C_d and the charge-transfer resistance R_{ct} according to the results from the first set of measurement. To confirm this, three similar sensors are measured in the second set of measurements simultaneously. However, no drop in sensitivity is observed till 45 days of measurement. At this stage, it is still not clear whether the correlation found in the first sensor was an outlier or not. Since no similar sensitivity drop is observed in the current 3 sensors, this implies that the abrupt drop happened to sensor No. 0 in the first set of measurement could be an outlier. The measurements will go on until the sensitivity drop is observed, when the EIS results may clarify the correlations found for the first sensor.

Acknowledgment

FIRSTLY , I would like to express my sincere gratitude to my supervisor Dr. Pantelis for providing me the opportunity to get in touch with the bio-tech field of electronics for glucose sensing.

Beside, I would like to thank my co-supervisor Dr. Ghoreishizadeh for her patience, enthusiasm and encouragement over the past months. Her continuous support and absolute dedication helps me in all the time of research and writing of this thesis.

I would also like to thank Dr. Sharma for his knowledge in electrochemistry, which helps a lot when I commenced studying the brand-new subject. His motivation and optimism really cheers me up.

My sincere thanks also goes to Prof. Anthony Cass for discussing and anylising the results with me.

Besides my supervisors, I would like to thank those who work in the lab for their stimulation, discussion and encouragement: Nicolas Moser, Khalid Mirza, Daiwen Sun, Lirui Zhang and Ze Ren.

Last but not the least, I would like to thank my parents, for giving birth to me and supporting me throughout my study.

Contents

List of Figures

List of Tables

Abbreviations

IMD:	Implantable Medical Devices
CYP:	Cytochrome P450
redox:	Reduction-oxidation Reaction
GOx:	glucose oxidase enzyme
EIS:	Electrochemical Impedance Spectroscopy
SOC:	System on Chip
WE:	Working Electrode
CE:	Counter Electrode
RE:	Reference Electrode
TIA:	Trans-impedance Amplifier
PBS:	Phosphate Buffered Saline
CPE:	Constant Phase Element

Chapter 1

Introduction

1.1 Medical Application Motivation

METABOLITES generally refer to the intermediates and products of metabolism of organisms. In a narrow sense, it is usually restricted to two categories of small molecules in human body metabolism, endogenous and exogenous ones.

It is a great necessity that human metabolites are monitored for modern personalised medicine [2]. As a matter of fact, many metabolic diseases with critical and/or chronic syndromes can be anticipated or discovered through monitoring means of endogenous metabolites while exogenous metabolism monitoring can be utilised to adjust the treatments (most frequently, the pharmacological dose) of various patients as individuals may respond differently to identical therapy [3].

The endogenous metabolism was defined by Lamanna, in 1963 [4], as the sum of all internal chemical activities executed by organisms without the existance of any utilisable external (of cells) substances for their energy absorption and growth. Among such metabolites involved, *glucose*, *lactate*, *glutamate* and *cholesterol* attract the most attention.

The concentration of glucose in human blood, which is often introduced as blood sugar, is a visible probe for diabetes while lactic acid appears in blood as a result of anaerobic metabolism in the absence of insufficient oxygen delivered to the tissues in severe
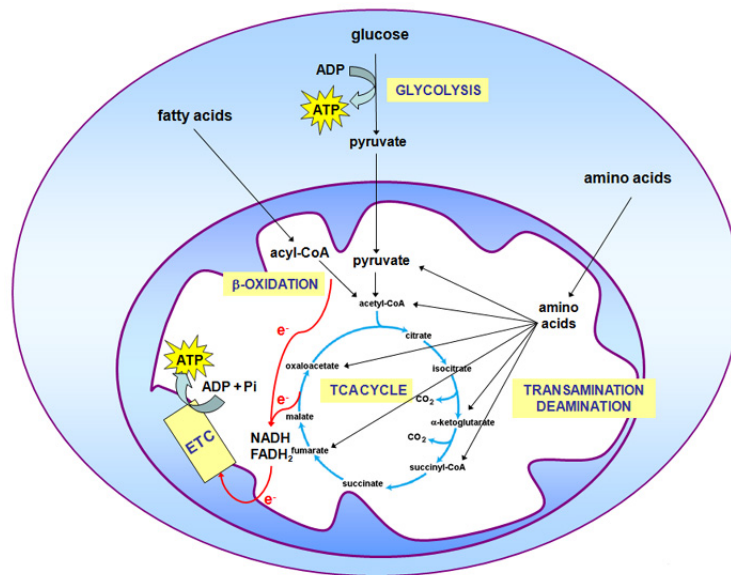
Figure 1.1: **Multiple entries of oxidative metabolism for fuel molecules like glucose and fatty acids [1].**

exercises or diseases. Glutamate in human body generally functions as the transmitter of neurons but in the case or brain injuries, it may accumulates outside the neurons and cause damage eventually. cholesterol is an essential component of cell construction, however, excessive high concentration in blood will partially contributed to arterial hypertension and atherosclerosis [5].

Many of the exogenous metabolites are typically associated with molecules involved in therapy, where the most interesting ones are $etoposide$, $ftorafur$, $cyclophospamide$, $ifosfamide$, etc. and they normally come from drug compounds used in patient treatment [5]. As a result, the level of exogenous metabolites in blood helps the monitoring of patients' response and later metabolising of the drug supplied. In this thesis, the targeted metabolite is glucose which appears in blood and plays an essential part in human body metabolism.

1.2 The Research Problem

Currently, the major drawback of the commercially available models of CGM sensors is its constant need for calibration due to changes its sensitivity over time. A calibration

step is thus needed with a finger-stick test at least once a day to get reliable and accurate results. Every time of calibration needs a finger-stick test (which is essentially performed by conducting the entire process of chronoamperometry measurement) which takes extra time and causes inconvenience for the patients relying on the sensors. Therefore, it is necessary to develop new approaches to simplify conventional calibration process at both lower cost and time-consumption.

This thesis aims to study the impedance of the sensor over time in an attempt to develop a new algorithm to predict the sensor performance. Instead of conducting an extra chronoamperometry session for calibration, EIS will be carried out to realise an auto-calibration of the glucose monitoring sensor. In particular, this research studies the correlation of the impedance with sensor sensitivity over time.

Chapter 2

Background Information

2.1   Electrochemical Fundamentals

ENZYMES are biological substances that act as catalysts in particular chemical reactions which could accelerate their rate in order to sustain the life of organisms [6] [7] [8].

Consequently, enzymes (mainly are essentially protein) can be utilised as biochemical marker for measuring the level of both endogenous and exogenous metabolites in human body. Specifically, endogenous compounds can be catalysed by the protein category of oxidases (typically redox reactions in organisms) as cytochromes P450 (CYP) are typically the tool for detecting exogenous molecules [5].

Since the focus of this thesis is on the glucose sensing hence the oxidases, which generally catalyses oxidation-reduction reactions would be studied. This type of biochemical reactions often involve singlet oxygen (O_2) as the oxidisers (accepting electrons) and are often reduced to water (H_2O) or hydrogen peroxide (H_2O_2).

Despite the fact that glucose oxidase is not an extremely specific type of catalyst, it is still more effective on glucose than on other kinds of sugars [9]. The reaction of glucose, $C_6H_{12}O_6$, oxidised by O_2 results in glucono-δ-lactone, $C_6H_{10}O_6$, and hydrogen peroxide, H_2O_2:

$$C_6H_{12}O_6 + O_2 \rightarrow C_6H_{10}O_6 + H_2O_2 \tag{2.1}$$
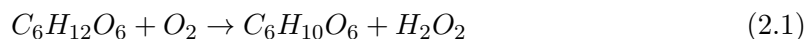
Normally, when in aqueous solutions, glucono-δ-lactone, $C_6H_{10}O_6$ would react with water simultaneously as the reaction in equation 2.1 happens, which generates gluconic acid, $C_6H_{12}O_7$. Hence the overall reaction can be represented as:

$$C_6H_{12}O_6 + H_2O + O_2 \rightarrow C_6H_{12}O_7 + H_2O_2 \tag{2.2}$$
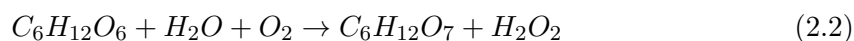
Enzymes like glucose oxidase (GOx, also known as notatin) normally have the products which can be measured with electrodes at the potential of $+550mV$ (the oxidation potential) [10]. As a result, it is feasible to apply constant potential to the electrode and recording the corresponding electrodes current, in order to monitor the redox reaction happening in the cell.

The readout during the redox process, is normally regarded to be proportional to the real-time level of glucose metabolised by using its corresponding enzyme (GOx) [5]. And the technique is named *chronoamperometry* due to the fact that the current (with unit Ampere) in electrode is recorded versus time (with prefix chrono-).

Another widely-acknowledged methods to study the behaviours of the electrochemical process happening the cell was called electrochemical impedance spectroscopy (EIS), which is based on the electric circuit modelling of the electrochemical cell (discussed in the next chapter). This electric approximation consists of pure as well as some frequency-dependent resistor and capacitor elements which can be measured with instruments by sweeping the frequency in a certain range.

As using biosensors with specific enzymes are a common way to measure metabolites. The next section will focus on the electrochemical sensors.

2.2   Previous Designs of Electrochemical Sensors

In recent years, with blooming modern technology in multiple multidisciplinary areas such as micro-sensors and bio-compatible materials sheds some light on developing bio-medical solutions for health care, cooperating with electronic measurements conducting by SoC solutions [11]. To be more specifically, advances in technology integration of electronics and medicine gives rise to some bio-medical solutions (biosensors) which are competent to monitor, and treat syndromes by sensing and measuring potential causing agents inside human body [12].

According to [13], a biosensor could be defined as an analytical device, which is capable of integrating a biological identification element closely with a paired transducer in order to supply a sensing system with the real-time conditions of the target analyte, such as its concentration.

Currently, a variety of different electrochemical biosensors are available in the market, which can be classified into four major categories: enzyme sensors, immunosensors, DNA sensors and ion channel sensors. In spite of these categories, all of the sensors are essentially constituted of a device with the functionality of recognise biological substances (or called a bioreceptor), which causes the bio-chemical reactions happening with the targeted analyte and leads to some specific kinds of manner to be detected and controlled by a signal transducer [14]. As a result, the foundation of a majority of biochemical sensors lies on the fabrication of biological components on multiple conductive and semi-conductive surfaces.

The glucose monitoring sensor, which is one type of enzyme sensors, is the one to be discussed in this thesis. This category of biochemical sensors are designed and built on the basis of the immobilisation of one certain kind of enzyme onto an manufactured electrode. The electrode can either be a metal one, which is employed in amperometric measurement (such as the monitoring of catalysed glucose oxidation with the enzyme as catalyst) or an ISE one, which is used in potentiometric measurement (such as the monitoring of catalysed release of hydronium/ammonium ions) [14].

The study on biochemical sensors based on enzymes (glucose oxidase, GOx) in application for the monitoring of blood sugar in human body is one of the important areas in biosensor development, in which the sensor materials constitutes a crucial part. This is due to the fact that development in material would enable the performance of a sensor to be improved so that the effect of general adsorption cause by irrelevant particles could be minimised.

To be specific, the design of biochemical sensors which is capable of both real-time and long-term monitoring of the glucose level in human blood requires the prohibition of the sensor surface reacting with interfering substances [14]. Recently, the study carried out by Gill [15] has claimed that the rate of sensor fouling could be inhibited by coating the membrane with substances such as macromolecules. Electrochemical impedance spectroscopy (EIS, which will be discussed in the following section) could be employed to characterise and evaluate the response of a biosensor (in reaction), which had been covered by a conductive polymer loaded with avidin [15].

Meanwhile, attentions have been drawn on the development of biosensors with micro electrodes, which are for the use in environmental and biomedical applications [16]. It worth noting that micro-electrodes have the ability to lower the requirements of detection/monitoring while greatly reduce the original response times [17].

Lately, the attempt to fabricate a micro-electrode array for enzyme-based glucose detection by sonochemical ablation has been made. It was shown in [18] that by ablating a polymer thin-film on an electrode surface with sonochemical approach would expose an area that may act like a micro-electrode, and multiple such kind of localised areas constitute a micro-electrode array. Besides that, EIS measurement is also adopted to measure and evaluate the performance of a sensor based on redox reactions. The impedance values changes in varying concentrations of glucose solution is justified by the activity of GOx [18].

Moreover, it is demonstrated in literature that both diffusion and kinetic control works in the process of charge transfer of a biosensor modified with gold for glucose detection. GOx is bound together with a Au nanoparticle covered by cystamine covalently,

then the glucose oxidase would be immobilised and attached to a gold electrode which is modified by dithiol. After that, EIS is employed to measure and evauate diffenrent stages of immobilisation [19].

As described in this section, researches have been conducted for years on developing various approaches for realisation of amperometric bio-sensor configurations [20] [21]. The following discussion will focus on the electrodes and the potentiostat with multiple current readout stages of a glucose biosensor.

2.2.1 Considerations on the Electrodes

Since in this thesis, the targeted metabolite is subcutaneous glucose, implementation of bio-medical sensors which utilises enzyme glucose oxidase to sensing the blood sugar, with electrodes are to be designed and developed. A constant electric potential should be applied to the electrochemical cell in order to maintain the redox reaction happen in a constant rate. Meanwhile, electrons flows would be measured as a current and then interpreted into glucose concentration.

To conduct the specified measurements, configurations with three electrodes are required. The first one is called *working electrode*, WE, which applies the desired, constant potential to the electrochemical cell and facilitates the redox reaction with electrons transmission. The *reference electrode*, RE, and the *counter electrode*, CE, functions as the other half of the reaction where RE provides a voltage as a reference of the WE to ensure the constant potential in WE. Meanwhile, the CE works to balance the charge equilibrium in the cell that supply or accept the electrons which are gained or lost by the working electrode.

2.2.2 Potentiostat with the Current Read-out Stage

The potentiostat circuit is essential in the modern electrochemical measurement system which functions to ensure the potential between WE and RE static (a constant value) as mentioned in the previous section. It is worth noting that the certain potential could be either fixed or configurable with respect to the ground [5]. Besides, measurement of the
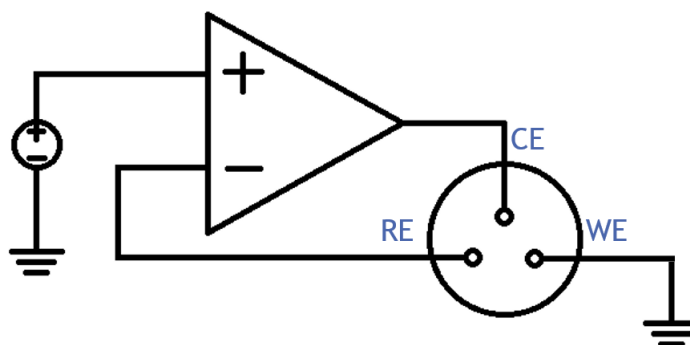
Figure 2.1: A theoretical diagram of potentiostat with three-electrode based electrochemical cell

current passing through WE should also conducted by the circuit.

Figure 2.1 shows a simplified circuit configuration of the potentiostat structure with a three-electrode cell where the working electrode is ground. This is one of the two possible configurations (the other is the grounded CE one). The current of cell, I_{cell}, is flowing in WE-CE pair while the voltage, V_{cell}, is measured between WE-RE pair. As described in the figure, an operational amplifier, which is named the driving amplifier, or potential control amplifier, works to alter I_{cell} hence the potential difference V_{cell} is able to maintain at the desired input potential level.

The current through WE can be measured easily by applying a simple configuration of a trans-impedance amplifier (TIA) with a certain value of parallel resistance (the gain) between the electrode and the ground hence the current is transferred to voltage and read out by the following stage.

Chapter 3

Literature Review

3.1 Existing Models of Electrochemical Cell

G ENERALLY , an electrochemical cell system could be interpreted by its impedance measured under the excitation of a sinusoidal signal with relatively small amplitude. As a result, the cell itself can be modelled according to its impedance with an equivalent circuit comprising resistors and capacitors that is able to pass through current of the same amplitude and phase characters as the electrochemical cell does in reality to the identical excitation [2].

The Randles equivalent circuit [22] is the most frequently used circuit among the existing models. It is a practical way of approximating an electrochemical cell into the representation of an electric circuit, as shown in Figure 3.1.

The parallel structure is introduced according to [23] due to the fact that the total current passing the working interface is contributed by the double-layer charging, i_c, and the faradaic process, i_f, simultaneously.

The total circuit consists of four basic elements. Resistor R_Ω or R_π, representing the resistance of the solution (mainly the electrolyte inside), where both currents branches pass through. The interface of electrode and electrolyte is symbolised by a nearly pure capacitor C_d or C_{dl}, which stands for the double-layer capacitance [24].

The faradaic process (lower part of Figure 3.1) can not be explicitly represented
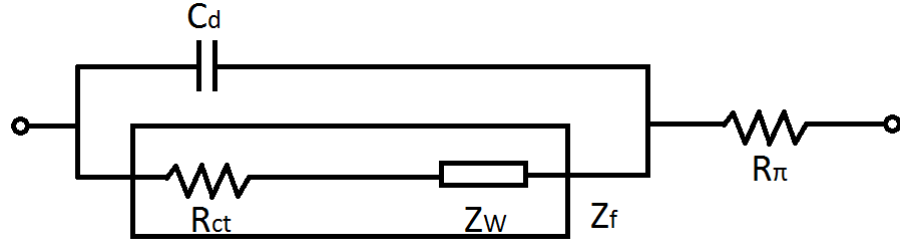
Figure 3.1: The typical Randles equivalent model for an electrochemical cell.

by pure resistors or capacitors since the values of the elements are dependent on on the frequency. As a result, it must be considered as a general impedance Z_f [23].

The faradaic impedance Z_f considered in literature are interpreted in several ways, among which the most straight-forward one is proposed by [25] that it can be represented by a series resistance, R_s, and the pseudo-capacitance, C_s in series. An alternative, which is also the model that is being adopted in this thesis, is to consider this general impedance as a serial combination consisting of a pure resistance, R_{ct}, the charge-transfer (resulting from the oxygen reduction reaction) resistance and Z_w, the 'Warburg' impedance, which to some degree stands for the resistance to mass transfer process [2].

Discussion on the faradaic process has been made in literature [26], elements in the frequency-dependent Warburg impedance (represented by two frequency-dependent elements R_w and C_w in series) can be expressed as equations 3.1:

$$Z_w = R_w + \frac{1}{j\omega \cdot C_w} \tag{3.1}$$

where

$$R_w = \sigma\omega^{-1/2} \tag{3.2}$$

$$Z_{C_w} = -j/(\omega C_w) = -j/(\sigma\omega^{-1/2}) \tag{3.3}$$

In equations 3.2 and 3.3, σ stands for the *Warburg* coefficient. It is the diffusion coefficient of ions in corresponding electrolyte which has the unit of $\Omega{\cdot}s^{-1/2}$. Therefore, the real and imaginary impedance part expressions of the equivalent circuit can be represented as [2]:
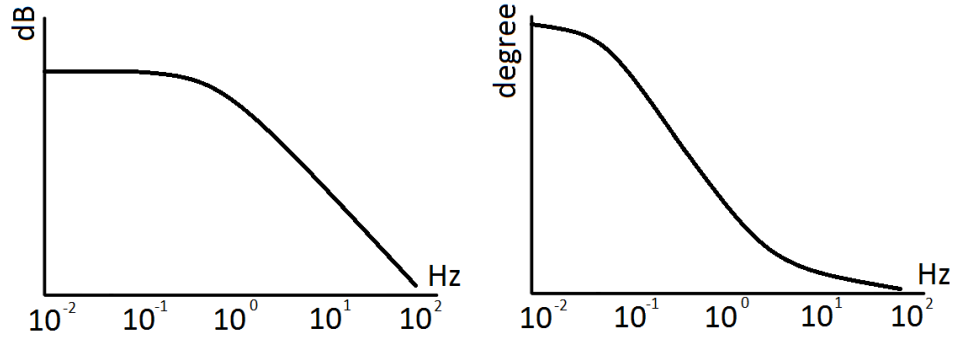
Figure 3.2: Simplified bode plots of a filter, impedance and phase vs frequency respectively

$$Z_{Re} = R_\Omega + \frac{R_{ct} + \sigma\omega^{-1/2}}{\omega^2 C_d^2 (R_{ct} + \sigma\omega^{-1/2})^2 + (C_d\sigma\omega^{1/2} + 1)^2} \tag{3.4}$$

$$Z_{Im} = \frac{\sigma\omega^{-1/2}(\omega^{1/2}C_d\sigma + 1) + \omega C_d(R_{ct} + \sigma\omega^{-1/2})^2}{\omega^2 C_d^2 (R_{ct} + \sigma\omega^{-1/2})^2 + (C_d\sigma\omega^{1/2} + 1)^2} \tag{3.5}$$

3.2   Method of EIS

In the previous sections of this chapter, the cell and approximation (Randles model) were introduced. However, electrical models or even more complicated ones [27] are only rough estimations of the electrochemical cells which may differ from what the real performances is.

As a result, to straight-forwardly investigate the impedance of cell in reality, direct measurement is of great necessity. As mentioned above, since the characteristics of faradaic impedance may vary from different frequencies, measurement with a wide range of frequencies (of AC component in input), typically from $1mHz$ to $1MHz$ [28], should be applied. The sweeping of frequency is exactly the reason why this kind of measurement of electrochemical cell is called Electrochemical Impedance Spectroscopy (EIS) or dielectric spectroscopy.

When varying the frequency of AC input signal, the performances can be assessed and illustrated in multiple ways. The conventional one of them is the Bode plots (shown in Figure 3.2), which plot the logarithm of the total impedance (typically in dB) $log(Z)$ as well as phase ϕ versus the logarithm of the frequency $log(\omega)$. Besides, a Nyquist plot

is adopted to complement the result as it presents the Z_{Im} vs Z_{Re}.

The Nyquist plots are extremely useful in impedance measurements, especially with frequency-dependent non-linear elements, because they could visualise the direct relationship between real and imaginary components of the targeted impedance. The following figures displayed displayed two fundamental cases, circuit with RC in series in Figure 3.3 a) and circuit with RC in parallel in Figure 3.3 b). Inductance is not considered here since the electrochemical cell only shows resistive and capacitive behaviours.
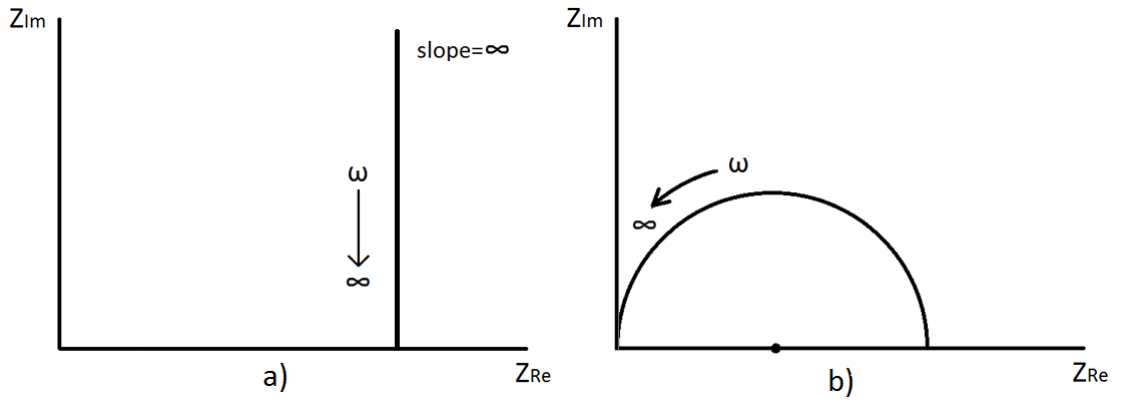
Figure 3.3: Basic cases of Nyquist plots, a) series RC circuit and b) parallel RC circuit

In this thesis, Randles equivalent model of the cell is adopted, as a result, Nyquist plots of the targeted circuit is desired. Theoretical deductions of both extreme frequency sides would be made for simplicity before the real measurements, where the focus should be on the frequency-dependent Warburg impedance.

When $\omega \rightarrow 0$, the expressions(equations 3.4 and 3.5) of real and imaginary impedance parts presented in previous sections can be simplified to [2]:

$$Z_{Re} = \sigma\omega^{-1/2} + R_{ct} + R_{\Omega} \tag{3.6}$$

$$Z_{Im} = 2\sigma^2 C_d + \sigma\omega^{-1/2} \tag{3.7}$$

Therefore,

$$Z_{Im} = Z_{Re} - R_{\Omega} - R_{ct} + 2\sigma^2 C_d \tag{3.8}$$

As a result, Z_{Im} vs Z_{Re} would be expressed linearly in this case. Moreover, the slope should be unity (shown in Figure 3.4). From the expression in 3.8, the interception point of the linear line with x-axis (real) is at $Z_{Re} = R_\Omega - R_{ct} + 2\sigma^2 C_d$ which would be useful in element value extraction from measurement results.
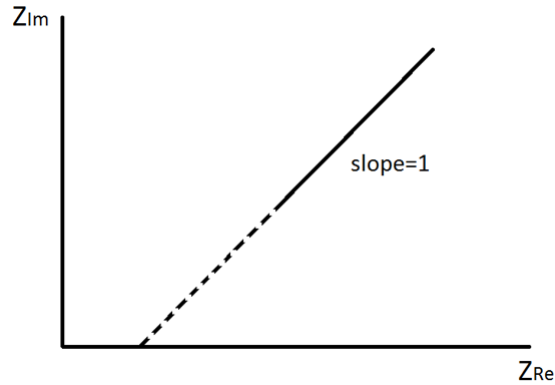
Figure 3.4: Nyquist plot for Randles Model at low frequencies

It is indicated from equation 3.8 that the only the Warburg impedance elements affect the shape of spectroscopy plot. As a result, the linearity is regarded as a behaviour of a process mainly controlled by diffusion (mass-transfer) [2].

It is worth noting that as the frequency increases, influence of double-layer capacitance C_{dl} would be more significant on the total impedance.

When ω is close to ∞, the Walburg elements becomes insignificant and the expressions of real and imaginary parts can be simplified to:

$$Z_{Re} = R_\Omega + \frac{R_{ct}}{1 + \omega^2 C_d^2 R_{ct}^2} \tag{3.9}$$

$$Z_{Im} = \frac{\omega C_d R_{ct}^2}{1 + \omega^2 C_d^2 R_{ct}^2} \tag{3.10}$$

Therefore,

$$\left(Z_{Re} - R_\Omega - \frac{R_{ct}}{2} \right)^2 + Z_{Im}^2 = \left(\frac{R_{ct}}{2} \right)^2 \tag{3.11}$$

Equation 3.11 indicated that the curve in Z_{Im} vs Z_{Re} plane would be a circle and can be illustrated in Figure 3.5.
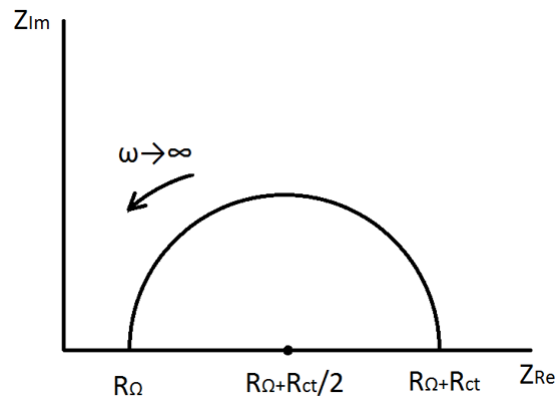
Figure 3.5: Nyquist plot for Randles Model at high frequencies

The semi-circle is centered at the point $Z_{Re} = R_\Omega + \frac{R_{ct}}{2}$ with radius equals to $\frac{R_{ct}}{2}$. Meanwhile, as the frequency approaches infinity, the total impedance would be near the value of pure solution resistance R_Ω.

Besides, according to the expression in equations 3.9 and 3.10, the frequency ω_0 value at the top of semi-circle can be deduced: $\omega_0 = \frac{1}{C_d R_{ct}}$.

By combining the two extreme cases, a rough curve for the whole frequency range can be illustrated, as shown in 3.6. This is the general shape of the results which are expected to been found in the experiment session.
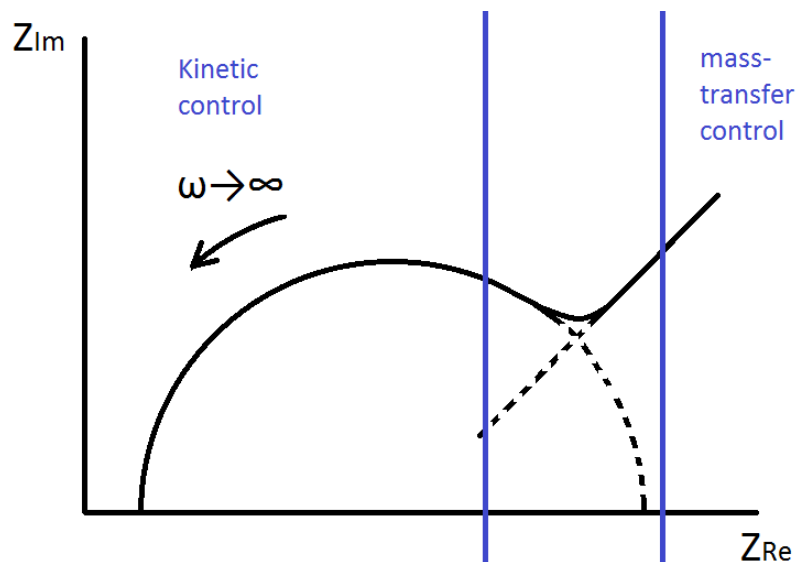
Figure 3.6: Nyquist plot for Randles Model

Chapter 4

Materials and Methods

4.1   Research Problem Revisited

AS mentioned in the introduction, the ultimate purpose in the thesis is to estimate the sensitivity directly from its EIS results without really carrying out the chronoamperometry measurement. Therefore, huge amount of data of results from both chronoamperometry and EIS measurements would be needed to find one or more possible forms of parameter correlations.

Measurements of sensors with chronoamperometry and EIS techniques would be conducted for the same sensor(s) for a period of time, which is nolmally longer than two weeks (14 days), the typically valid period for the targeted sensor. Afterwards, MATLAB algorithm and GUI to display and extract the values of parameters from EIS results to evaluate all of the equivalent circuit elements will be developed. With the data collected from the experiments, relationship between the parameters with the sensitivity would facilitates the development of auto-calibration algorithm.

Meanwhile, electric circuit would be designed to measure the sensor sensitivity with the impedance of an electrochemical sensor then combined with possibly micro-controller to enable the auto-calibration of sensor, as a fully implantable medical device.

4.2   Experimental Setup

4.2.1   Instruments Setup

The measurement session focuses on the performance of Enlite$^{\text{TM}}$ Glucose Sensor, one of the commercially available models of sensors for continuous glucose monitoring (shown in Figure 4.1), which is developed by Medtronic Ltd.

Figure 4.1: Enlite$^{\text{TM}}$ Glucose Sensor designed by Medtronic Ltd.

Meanwhile, in order to acquire the parameter data of sensor with relatively high accuracy, measurements in both chronoamperometry and EIS techniques are performed by CHI760E Electrochemical Workstation (shown in Figure 4.2) by CH Instruments, Inc, which integrated the functionality of potentiostat, galvanostat, impedance measurement and etc.

Figure 4.2: CHI760E Electrochemical Workstation by CH Instruments, Inc.

This model of general-purpose electrochemical measurement instruments possessed

matched WE, RE and CE configuration with the used sensor. In addition, it also provides a second WE for bipotentiostat measurements for multiple targeted metabolites.

The computerised display is performed with CHI version 13.12, which was revised on 28/10/2013. The software was operated in Windows XP$^{\text{TM}}$.

In the software GUI, techniques of Amperometric i-t Curve and A.C. Impedance are employed for the desired measurements. One of the two is chronoamperometric i-t curve.

The initial potential level, which represented the constant DC voltage applied to the sensor, was set to be $0.53V$. Run time was generally from 6000 to 10000 s. This is because the chronoamperometry measurement requires relatively longer time than EIS since the output current from the sensor need need time to settle down (which usually takes 30 to 60 minutes). Afterwards, concentration of glucose solution would be altered for several times and the sensor's responses would be recorded.

The other one of the two techniques employed was the electrochemical impedance spectroscopy (EIS).

The DC voltage level (init E) is set to be $0.53V$ for the enzyme on Enlite$^{\text{TM}}$ glucose sensor to take effect. In addition, an AC sinusoidal signal with amplitude $5mV$ is added to enable the spectroscopy. Frequency range of EIS is from $10Hz$ to $1MHz$ which covers both the kinetic and mass-transfer control regimes (semi-circle and linear parts) of the sensor.

It is worth noting that, in the setting, points per decade frequency for $100K-1MHz$ and $10K-100KHz$ are 19 while the other ranges are 12 (by default). This results from the fact that in high frequency range (the semi-circle part), distance between adjacent points are larger than in low frequency range (linear range). Therefore, it is necessary to obtain more points in this crucial range for better parameter extraction.

Impedance measurements for every sensor are conducted for multiple concentrations of glucose solution.

4.2.2 Solution Preparation

Phosphate buffered saline (PBS) is one kind of aqueous buffer solution which is essentially for biological and its interdisciplinary research. One of its most important features is that PBS has the same level of osmolality and ion concentrations as those in human body. Meanwhile, it is non-toxic to most cells. Varieties of buffer solutions such as PBS are normally used to rinse cells in immuno-histo-chemistry process and other cellular researches [29] [30] [31].

The formulations of PBS preparation can be different. Some don't introduce potassium yet some include calcium and/or magnesium. But generally it's most common recipe includes: sodium chloride, potassium chloride, disodium hydrogen phosphate and potassium dihydrogen phosphate [32].

The PBS solution used in this experimental session is made up with PBS tablets produced by Sigma Aldrich, which mainly consist of potassium chloride and sodium chloride. By dissolving one tablet into 200 mL of water makes 0.01 M phosphate buffer, which contains 0.0027 M potassium chloride and 0.137 M sodium chloride with pH value of around 7.4 at 25 $°C$. In this thesis, $100mM$ PBS solution was made with the tablets and distilled water.

Dextrose is the D-isomer of glucose which is commonly occurred in nature. The stock solution is made by dissolving Dextrose Monohydrate powder with empirical formula $C_6H_{12}O_6 \cdot H_2O$, produced by Sigma Aldrich into $100mM$ PBS solution.

In the first set of measurement, the stock solution has glucose concentration of $1M$ while in the second one, $100mM$ glucose solution is used.

After daily measurements, the sensors are ought to be stored in a similar environment where the real sensor will be use in real life. This environment is provided by the storage solution. In the first set of measurement, the storage solution are simply $20.0mM$ glucose solution while in the second one, $30mg/ml$ of albumin is added into $5.0mM$ glucose solution.

The addition of albumin into storage solution, is a further step to mimic the envi-

ronment, when metal (tip of the sensor) is inserted subcutaneously.

4.2.3   Measurements

The first set of measurements started in 5th April and ended in 19th May in 2016, totally lasted for 45 days while the Enlite$^{\text{TM}}$ glucose sensor was expected to be valid for around 2 weeks.

To monitor the output current from the cell (via potentiostat) in different concentration of glucose, the plan was to add fixed amount of (stock) glucose solution every five minutes to a beaker of relatively large volume of base PBS solution while the instrument is implementing the continuous measuring.

Figure 4.3: Base PBS solution in the beaker.

Base PBS solution was $12ml$ of $1M$ PBS solution solved in distilled water as mentioned in the previous section. The solution was contained in a cylinder glass beaker (as shown in Figure 4.3). To maintain the solution uniformly after adding glucose, a small magnetic-stirrer bar was also in the beaker and it would rotate when the magnetic stirrer, on which the beaker was sit, was turned on.

Moreover, it is essential to isolate the entire measuring setup from the potential electrostatic and electromagnetic influences in the surrounding environment. Therefore, a metal screen named Faraday Cage, was introduced in the experiment session to protect the devices(as shown in Figure 4.4).

Figure 4.4: The Faraday cage used in the measurement.

For the chronoamperometry part, it was planned to increase the glucose concentration in a step of $2.5mM$, by adding stock glucose solution into the beaker for 8 times till the concentration reached $20.0mM$.

$$N_1 V_1 = N_2 V_2 \tag{4.1}$$

hence

$$1000 \cdot x = 2.5 \cdot 12 \tag{4.2}$$

where

$$x = 0.03mL = 30\mu L \tag{4.3}$$

In equation 4.1, the left hand side stands for the glucose in stock solution added, while the right hand side represents the targeted amount of glucose. It is worth noting that the added volume is negligible compared to $12ml$, which is verified in the equation 4.3.

The result 4.3, indicates that $30\mu L$ of stock solution should be added every 5 minutes.

Besides the chronoamperometry, impedance measurement was also implemented every day, but for only two concentrations, which were $0.0mM$ and $20.0mM$. This is

because of the fact that, two different kinds of measurements can not be conducted simultaneously.

In this set of measurements, only one sensor was used and stored in the solution with final concentration $(20.0mM)$ for the sake of convenience. All the solution as well as the sensor were stored in the refrigerator between two days' measurements.

The second set of measurements started in 15th July and ended in 16th August in 2016, totally lasted for 33 days to ensure the measurement would cover the degrading of the Enlite^{TM} glucose sensor, which is normally 14 days. To make the results more reliable, three sensors were used in every day's measurement.

To acquire more data in EIS, impedance measurements were implemented in six concentrations of glucose solution, from 0 to $12.5mM$ with a step of $2.5mM$) after every time's chronoamperometry with the same sensor.

To simplify the operations, new containers were adopted:
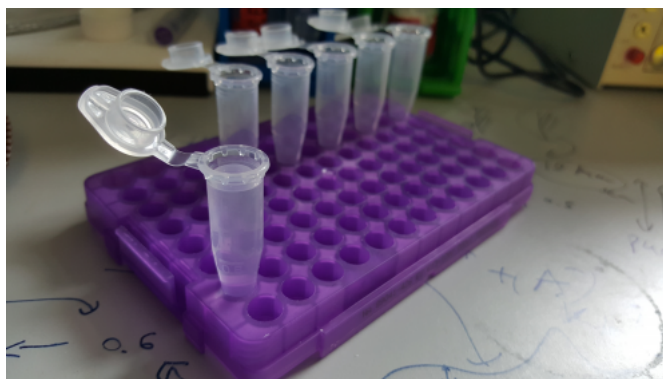
Figure 4.5: Centrifuge tubes manufactured by Corning Inc.

Multiple separated plastic centrifuge tubes were used to contain different concentration of glucose solution as shown in Figure 4.5.

Volumes of the solution in these $1.5mL$ tubes were actually $1.6mL$ (all identical) to ensure that same lengths of the tip of each sensor were dipped in to the solution. Since in this set of measurements, stock glucose solution had the concentration of $100mM$ (instead of previously used $1M$), the solution addition each time (to increase the concentration by $2.5mM$) could not be negligible any more.

To make six different tubes of glucose solution with concentration values required, detailed preparation ratios are shown in Table 4.1.

Targeted Glucose Concentration $/\mu L$	$100mM$ Glucose Stock Solution Needed $/\mu L$	$100mM$ PBS Solution Needed $/\mu L$	Total Volume $/\mu L$
0.0	0	1600	1600
2.5	40	1560	1600
5.0	80	1520	1600
7.5	120	1480	1600
10.0	160	1440	1600
12.5	200	1400	1600

Table 4.1: Solution preparation for 6 different concentrations

As shown in Figure 4.6, six tubes were located in adjacent holes of a plastic shelf. Concentration increasing can be implemented by moving the sensor from one tube to another after the tip of the sensor was washed by distilled water during chronoamperometry and EIS measurements.
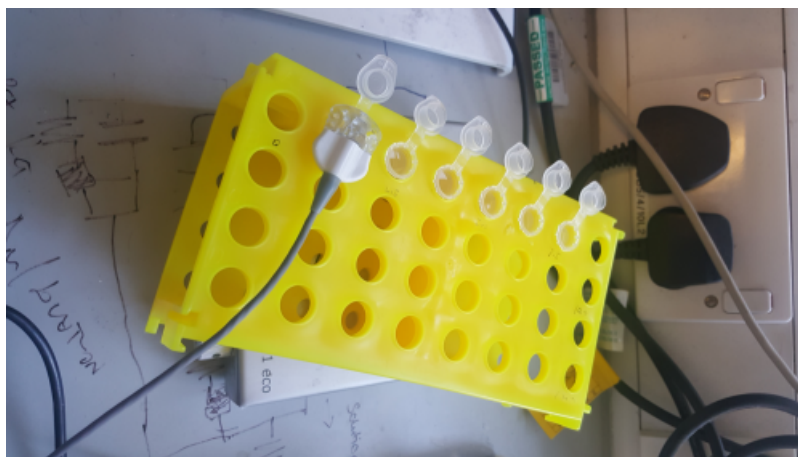
Figure 4.6: 6 sets of different concentration of glucose solution in measurements

The storage method was also improved. The sensors were stored in the environment where all the factors are more similar to those in real situation. Storage solution was redesigned where $5.0mM$ of glucose solution (closer to normal human blood sugar level) was adopted instead of $20mM$. In addition, the albumin powder was added into the glucose solution to mimic the situation where metal objects (tip of the sensor) is inserted

under skin.

Moreover, a specialised chamber which is capable of control the temperature and the humidity inside, was used to store the sensors between the measurements instead of the refrigerator.
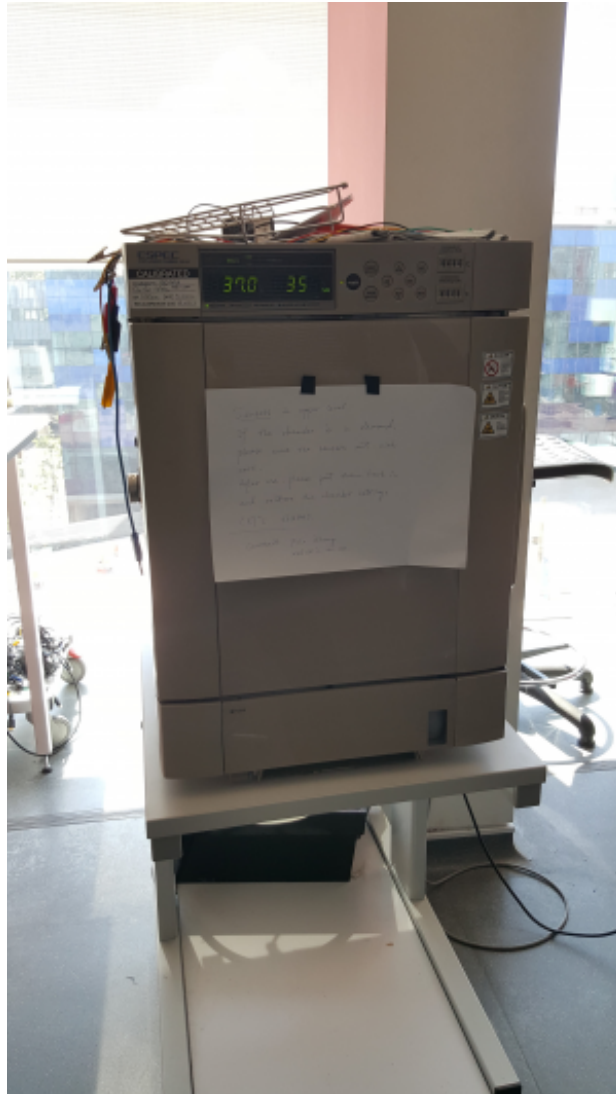
Figure 4.7: **Temperature and humidity chamber model SH221 manufactured by ESPEC**

As shown in Figure 4.7, the temperature was set to $37°C$ which is closer to the temperature of human body. The relative humidity was set to a relatively low condition to prevent the storage solution from being influenced by the vapor.

4.3   Data Extraction

The main purpose of this step is to extract the approximated values of each electric circuit elements shown in Figure 3.1). Specifically, the targeted parameters are R_π, the solution resistance, R_{ct}, the charge transfer resistance, C_d, the double-layer capacitance, k_{R_w}, the resistive parameter of Warburg impedance and k_{C_w}, the capacitive parameter of Warburg impedance. Moreover, to verify the estimated value of sensitivity, the original value should also be extracted from the raw data.
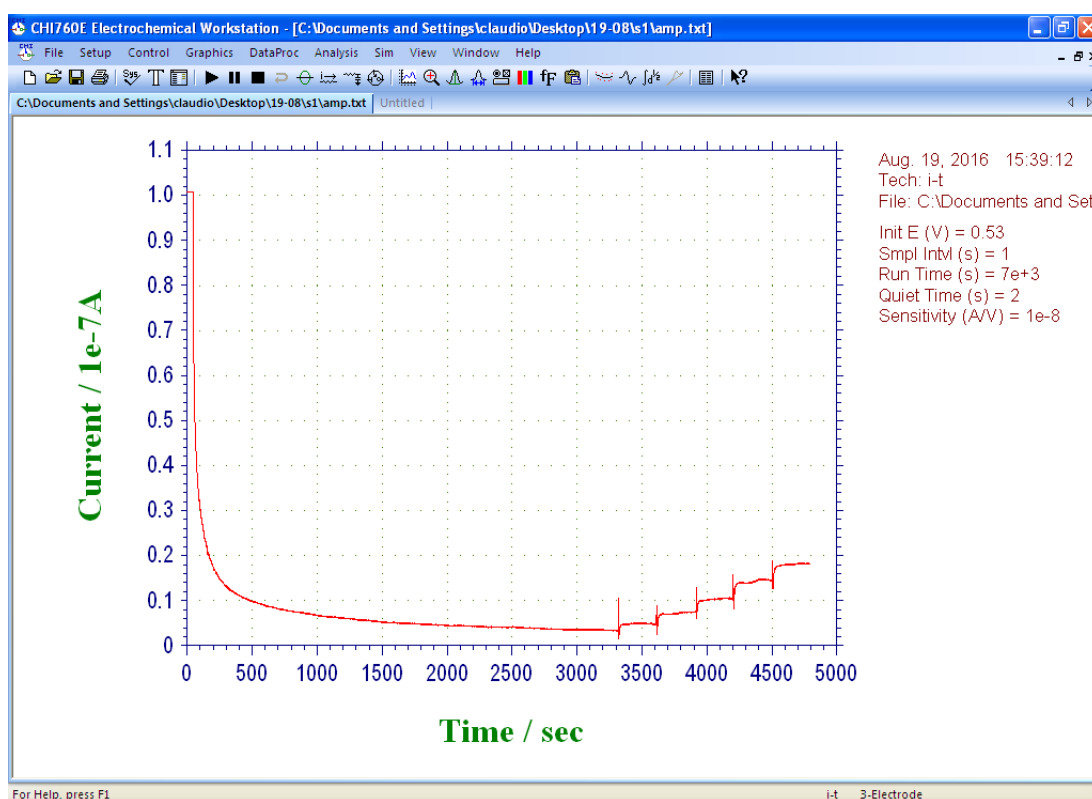
Figure 4.8: **Original results from i-t technique displayed in CH Instrument software**

As shown in Figure 4.8, after implementing a chronoamperometry measurements, the result of output current versus time would be available. Every time the concentration was increased by changing the tube that the sensor was dipped into, there would be a step which lasted for approximately 5 minutes. It is also worth noting that when switching the tube, when the tip of sensor was floating in air (not inside the solution), there would be sharp impulse (shown in-between the steps).

In this case shown above, the value would be evaluated from $3200 - 3300s$, $3500 - 3600s$, $3800 - 3900s$, $4100 - 4200s$, $4400 - 4500s$ and $4700 - 4800s$, where data from only the final $100s$ from each step were used to estimate the average value for a certain concentration. Then the result would be plotted in a current vs. concentration, which is plotted in Microsoft Office Excel and displayed in Figure 4.9.
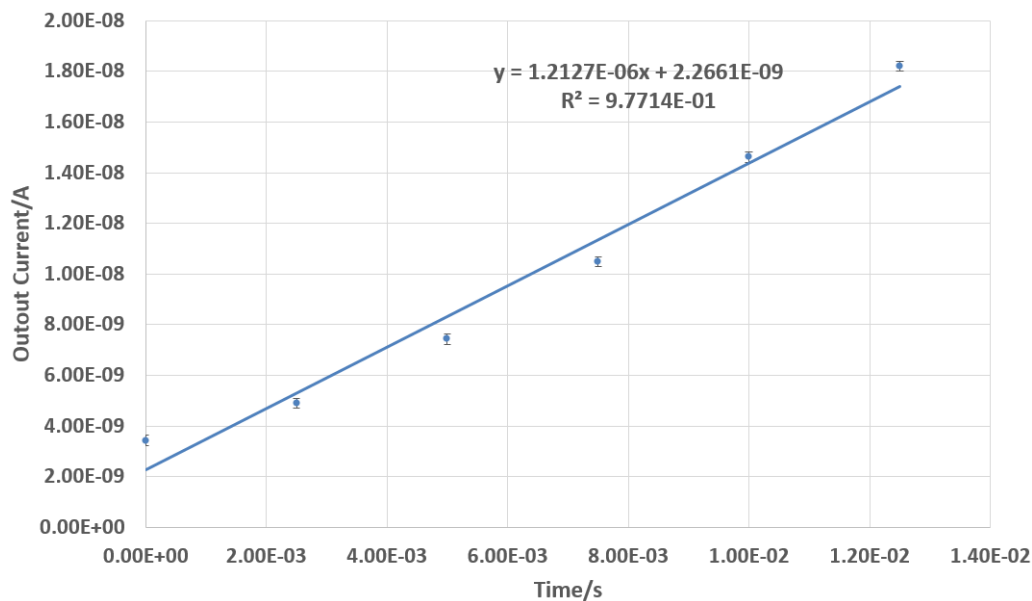
Figure 4.9: Output current vs. glucose concentration plotted with data from Figure 4.8

It is indicated in Figure 4.9 that the output current is not always directly proportional to the glucose concentration as expected (the solid line). Since the value of its sensitivity is defined to be the slope of the expected straight line (from current vs. concentration), it is not realistic to obtain its value by simply connecting all the points.

One of the possible solution is to draw the linear regression line (represented in dotted line) produced from these six points. In this case, the value of sensitivity, which is also known as the m value, could be obtained from the dotted line's slope, which is $1.2127 \times 10^{-6} A/M$. In Figure 4.9, the vertical error is set to be $2 \times 10^{-10} A$, which is obtained from the standard deviation of data for each point.

Meanwhile, for the EIS measurements, same software GUI provided by CH Instrument was used. As shown in Figure 4.10, after implementing an EIS measurements, the results of Bode plots are displayed in the software GUI where $log(impedance)$ vs.
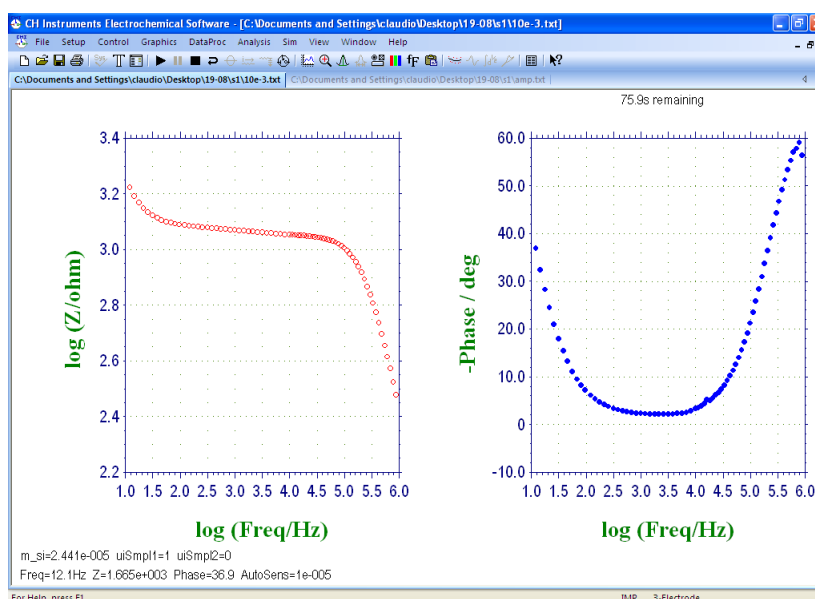
Figure 4.10: **Original results from EIS technique displayed as Bode plots**

$log(frequency)$ is on the left while on the right side is the plot of *phase* vs. $log(frequency)$.
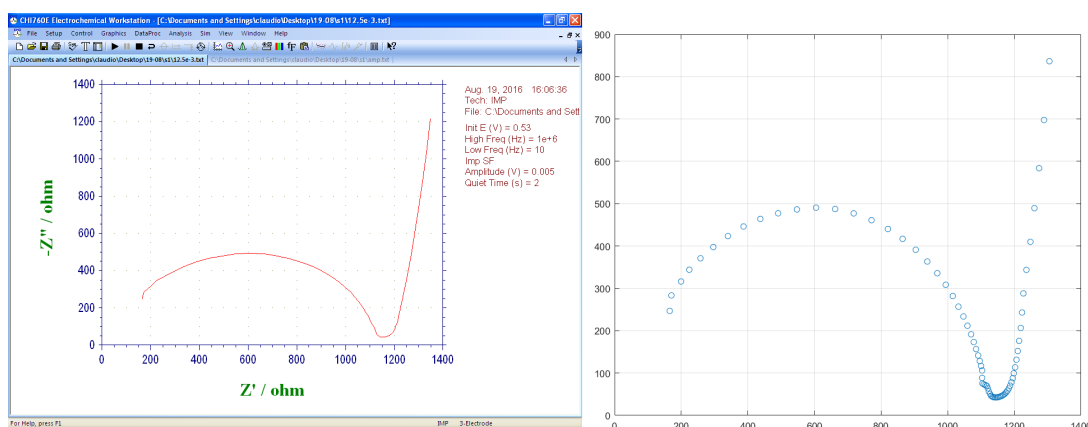
Figure 4.11: **Result from EIS technique as Nyquist plot in CHI software and MATLAB**

An alternative to display the result is the Nyquist plot (shown in Figure 4.11). The same sets of data are plotted in (minus) imaginary part versus real part of the total impedance, both in both CH Instrument software and MATLAB. The shape is essentially a semi-circle connected to a straight line as predicted in Figure 3.6 in the previous section.

Algorithm of parameter extraction consists of two main parts: circle fitting and linear regression.

As discussed in the previous chapter, data in the high frequency regime constitute an arc in a circle of which the center is located on the real axis at $Z_{Re} = R_{\Omega} + \frac{R_{ct}}{2}$ with radius equals to $\frac{R_{ct}}{2}$. By fitting this part of the curve, it would be relatively straightforward to obtain the value of resistance R_{Ω} and R_{ct} by simply calculating the interception points of the fitted circle with the real axis.

Fitting a circle (or circular arc) to a known series of data points is essential in areas such as statistics, computer graphics, nuclear physics, petroleum engineering an etc [33] [34].
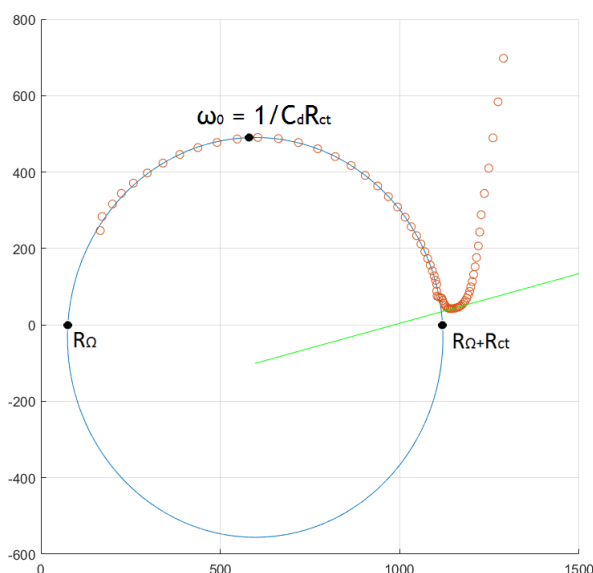
Figure 4.12: Result graph after parameter extraction in MATLAB

Till now, algorithms to fit circular arcs or whole circles to data points have been developed. These algorithms can be generally categorised into to types: geometric fits which emphasise the minimisation of geometric distances from the data points to the resultant circles/arcs, while algebraic fits which aim to minimise the valve of some specific terms of so-called distances [35]. Error analysis by [35] focused on some of the most popular algorithms, including geometric and Kasa, Pratt, Taubin from algebraic fits, concludes that the method introduced by R. Taubin [36] fits circles with smaller essential bias than Kasa and Pratt hence has a better performance overall. As a result, a MATLAB version of Taubin circle fitting is adopted in the parameter extraction.

As shown in Figure 4.12, the circle in blue solid line is fitted to the data points at high frequency regime. Specifically, the 9th to the 28th points, 20 points in total are used in the fitting. It is worth noting that the curvatures of the shape from raw data points at the highest frequencies (several points on the left) varies a lot, hence the circle fitting are located a bit to right hand side to ensure a better performance.

After completing the circle fitting, with the value of charge transfer resistance, R_{ct}, it is also relatively straight forward to acquire the double layer capacitance C_d, from the highest point in the circle where the corresponding frequency $\omega_0 = \frac{1}{C_d R_{ct}}$.

The problems comes from the location of the desired point as it is not always the case that the discrete points recorded form the spectroscopy covers exactly the highest point. Three methods are developed and used here to estimate the points and then the mean value is adopted in parameter extraction.

The simplest approach is to select the closer one of the two points (acquired by EIS) as the highest point by a double for-loop.
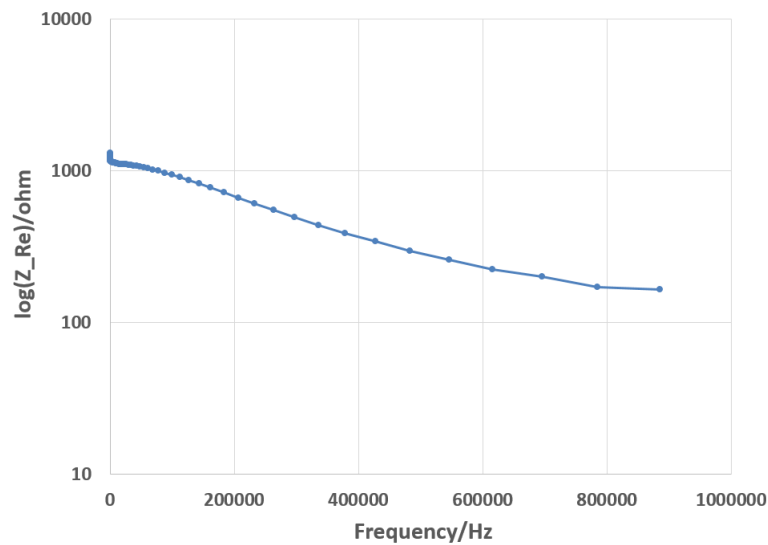
Figure 4.13: $log(Z_{Re})$ **vs. the frequency general trend**

The second method is implemented by the linear regression on the relationship between $log(Z_{Re})$ vs. the frequency. As shown in Figure 4.13, at high frequency range, these two parameters are relatively close to a linear relation. As a result, frequency of

the point with desired x-coordinate (which can be determined by the circle centre) can be used as ω_0.
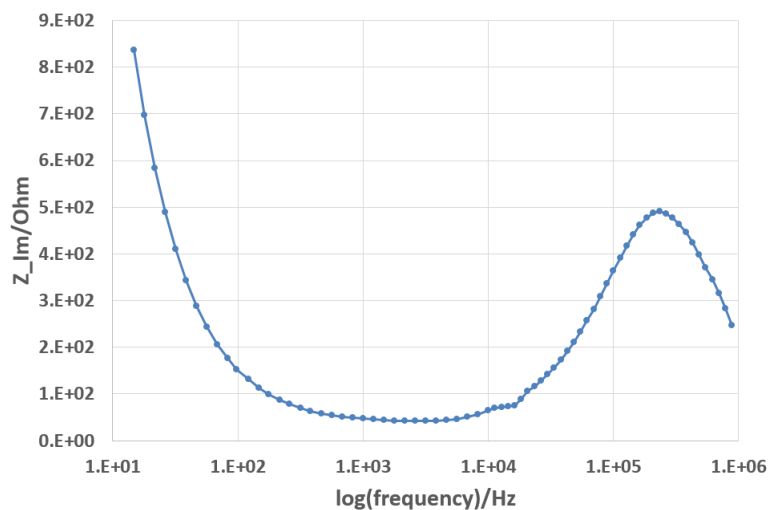
Figure 4.14: Z_{Im} **vs. the** $log(frequency)$ **general trend**

The third method is realised by a second-order polyminial curve fitting to the same range of data points. This results from the fact that Z_{Im} vs. $log(frequency)$ looks similar to a second order polynomial relation at high frequency range (as shown in Figure 4.14). As a result, the desired value of frequency, ω_0, can be obtained by solving the second-order equation.

After implementing these three methods, the mean value of ω_0 is then used to calculate the capacitor C_d.

The other part of the algorithm is the linear fitting of the lower range of frequency part of data points. As shown in Figure 4.12, the straight line in solid green is fitted to, specifically, the 43rd to the 49th points, 7 points in total. It is worth emphasising that the deductions of parameters k_{R_w}, the resistive parameter of Warburg impedance and k_{C_w}, the capacitive parameter of Warburg impedance are based on the interception point of the fitted straight line with the real-axis. Meanwhile, this interception point should be inside the fitted circle.

The MATLAB codes used for data extraction can be found in the Appendix.

Chapter 5

Experiment Results

5.1 Long-term Sensor Sensitivity Measurement

I N this section, the results from both sets of experimental measurements, the first from April to May, 2016 while the second from July to August, 2016, would be presented.

5.1.1 Results from Sensor No. 0
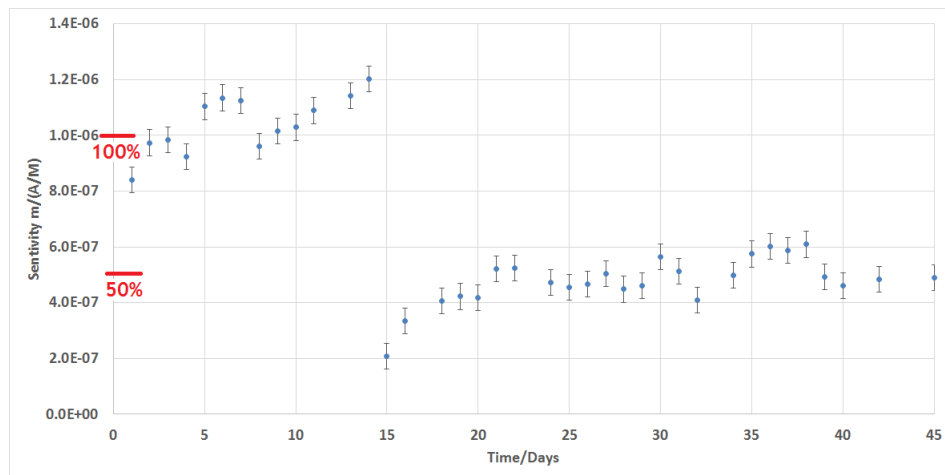
Figure 5.1: Sensor No. 0: Sensitivity vs. no. of days in 1st set of measurements

Figure 5.1 displays the value of sensitivity m versus time (in days). In the 1st set of measurement, sensor No.0 is measured for 45 days. The scatter plot shows a general trend that m stays constant in a certain range (around $1 \times 10^{-6} A/M$) then abruptly drops

to a much smaller one (around $5 \times 10^{-7} A/M$).
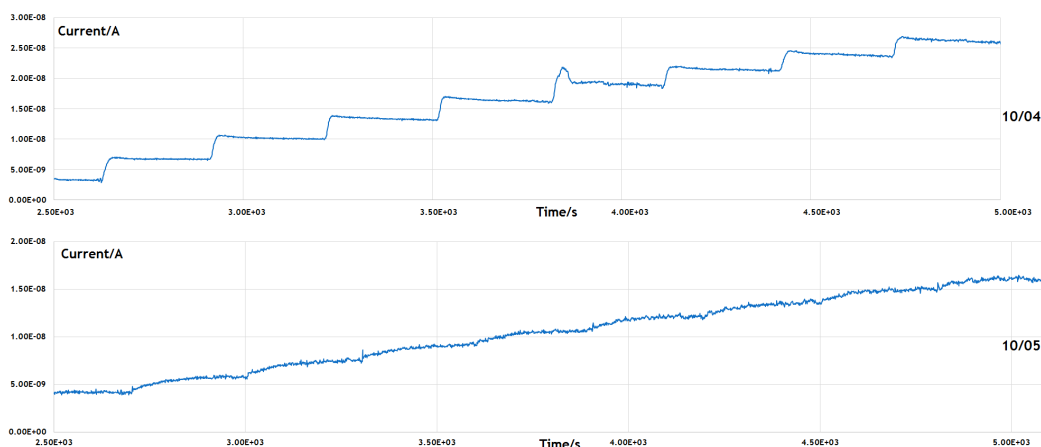
Figure 5.2: Sensor No. 0: current vs. time in two different days

This kind of change can be observed from the raw data from chronoamperometry curves, in which the heights of each step drops from approx. $3nA$/step (the 6th day) to $1.5nA$/step (the 36th day), as shown in Figure 5.2.

5.1.2   Results from Sensor No. 1 to 3
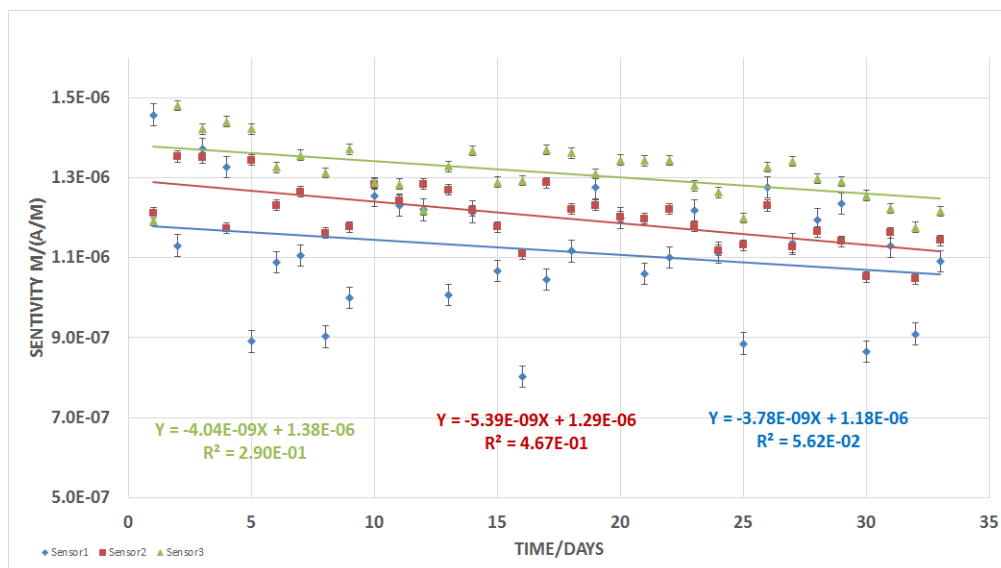
Figure 5.3: Sensor No. 1, 2 and 3: Sensitivity vs. no. of days in 2nd set of measurements

The 2nd set of measurement, which started at 15th July, 2016 and is still in progress,

measures three sensors numbered No. 1, 2 and 3 simultaneously. The analysis in this section focuses on the data acquired from the 1st to the 35th day.

As shown in Figure 5.3, the sensitivities of all three sensors do drops at some rates but still not yet 50% of their original values. Consequently, two clusters of data points are not expected from the extracted parameters.

Table 5.1: Sensitivity m Comparison of measured sensors

|	No. 0	1	2	3
Day 1	8.4094E-07	1.4572E-06	1.2113E-06	1.1921E-06
2	9.7338E-07	1.1303E-06	1.3530E-06	1.4800E-06
3	9.8454E-07	1.3716E-06	1.3495E-06	1.4218E-06
4	9.2382E-07	1.3272E-06	1.1734E-06	1.4402E-06
5	1.1034E-06	8.9020E-07	1.3440E-06	1.4220E-06
6	1.1343E-06	1.0892E-06	1.2312E-06	1.3256E-06
7	1.1252E-06	1.1050E-06	1.2645E-06	1.3562E-06
8	9.6013E-07	9.0210E-07	1.1610E-06	1.3123E-06
9	1.0164E-06	9.9880E-07	1.1767E-06	1.3715E-06
10	1.0286E-06	1.2544E-06	1.2839E-06	1.2872E-06
11	1.0890E-06	1.2313E-06	1.2434E-06	1.2843E-06
12	1.1420E-06	1.2197E-06	1.2838E-06	1.2179E-06
13	1.2025E-06	1.0068E-06	1.2691E-06	1.3281E-06
14	2.0804E-07	1.2145E-06	1.2178E-06	1.3678E-06
15	3.3341E-07	1.0676E-06	1.1771E-06	1.2890E-06
16	4.0593E-07	8.0310E-07	1.1099E-06	1.2931E-06
17	4.2204E-07	1.0450E-06	1.2870E-06	1.3701E-06
18	4.1841E-07	1.1164E-06	1.2210E-06	1.3619E-06
19	5.2202E-07	1.2752E-06	1.2306E-06	1.3101E-06
20	5.2470E-07	1.1991E-06	1.2026E-06	1.3441E-06
21	4.7261E-07	1.0597E-06	1.1974E-06	1.3426E-06
22	4.5473E-07	1.0999E-06	1.2216E-06	1.3435E-06
23	4.6744E-07	1.2179E-06	1.1791E-06	1.2798E-06
24	5.0297E-07	1.1132E-06	1.1185E-06	1.2631E-06
25	4.4805E-07	8.8517E-07	1.1308E-06	1.1994E-06
26	4.6105E-07	1.2759E-06	1.2303E-06	1.3263E-06
27	5.6398E-07	1.1340E-06	1.1269E-06	1.3412E-06
28	5.1296E-07	1.1954E-06	1.1648E-06	1.2980E-06
29	4.0845E-07	1.2356E-06	1.1407E-06	1.2908E-06
30	4.9911E-07	8.6428E-07	1.0523E-06	1.2555E-06

Table 5.1 displays the sensitivity values for all four sensors measured. Generally, the average value of sensitivity of No. 0 is smaller than the rest three. Meanwhile, sensor No. 0 displays a distinct decline in m value which is not observed for the rest three.

5.2   EIS Measurement

5.2.1   Results from Sensor No. 0
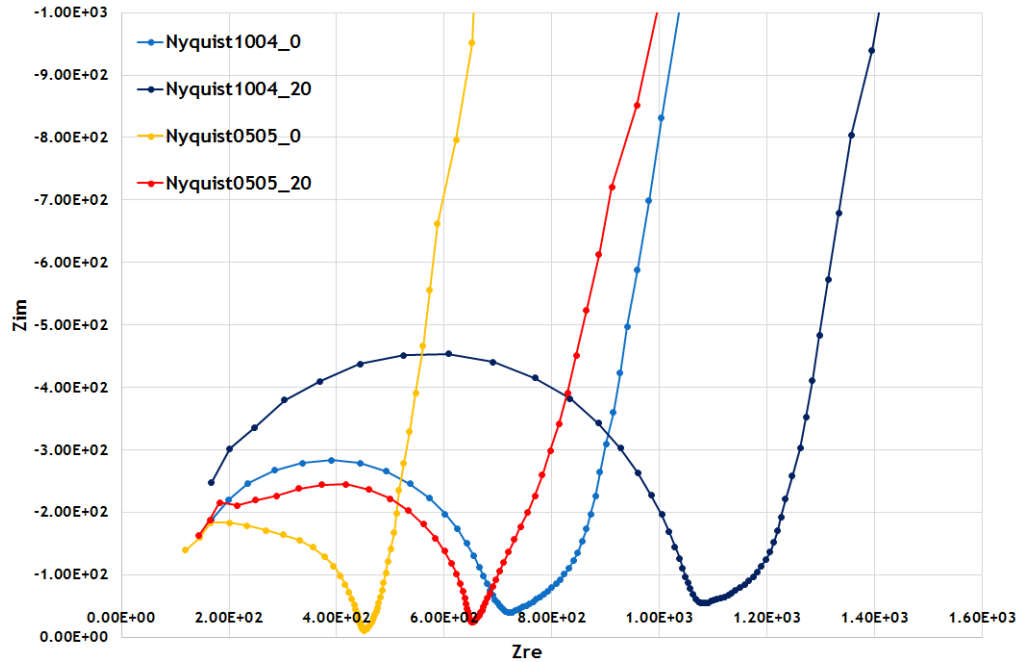
Figure 5.4: EIS results in Nyquist plots: yellow and red: day 10 (10-04), blue and navy: day 35 (05-05)

Figure 5.4 displays the Nyquist plots for both concentrations (0 and 20 mM) of sensor No. 0 at day 10 and day 35. The curves are plotted in Microsoft Office Excel.

It is implied from Figure 5.4 that, at the same day, when the concentration goes higher, radius of the semi-circle will increase as well, which indicates a visible growth in charge transfer resistance R_{ct}. When considering the same concentration fro different days, the radius increases as the measurement proceeding.

To summarise, the charge transfer Resistance R_{ct} appears to be correlated to the a) concentration of glucose solution, b) the number of measurement days.

5.2.2   Results from Sensor No. 1 to 3

Figure 5.5 shows the EIS results in Bode plots, which are the same as what are displayed in the CH Instruments software.
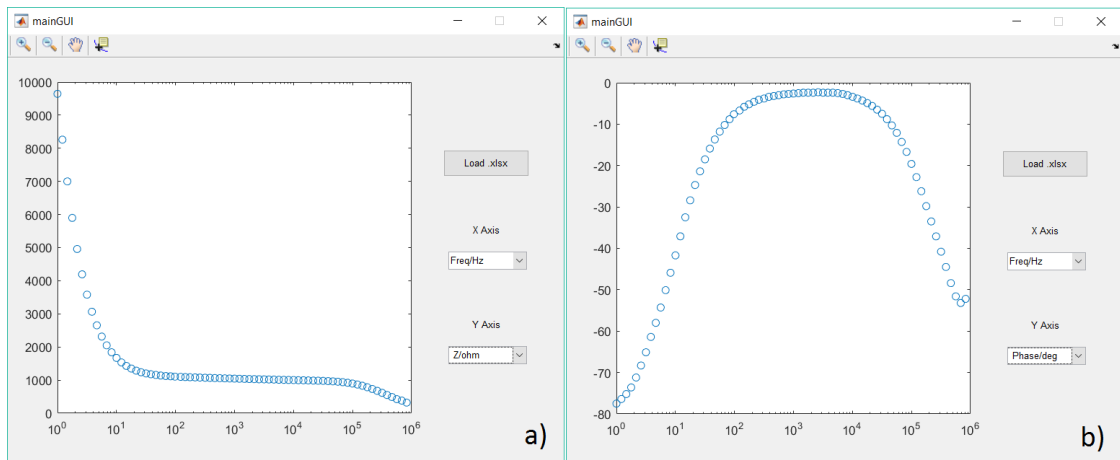
Figure 5.5: MATLAB GUI displaying the EIS raw data in Bode plots: a) Z_{total} vs. $log(frequency)$ b)$Phase$ vs. $log(frequency)$
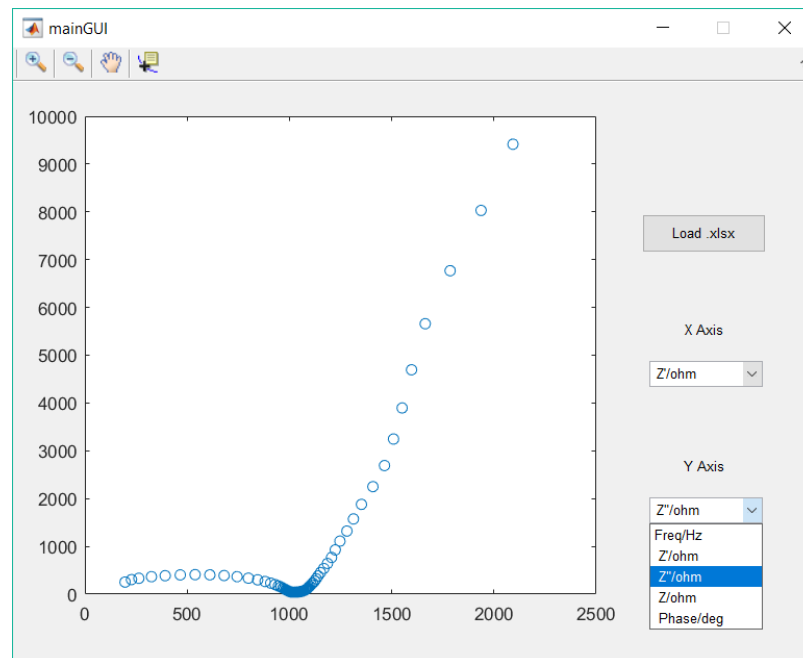
Figure 5.6: MATLAB GUI designed to display the EIS raw data $-Z_{Im}$ vs. Z_{Re}

The Bode plots are then transferred to a Nyquist plot (shown in Figure 5.6), in order to perform the parameter extraction. By performing the circle fitting with the linear regression in the Nyquist plots, the parameters are extracted:

Table 5.2: Parameter Extraction for Sensor No. 3 in 7.5 mM glucose solution

Date	Time/Days	Rpi/Ohm	Rct/ohm	Cd/F	k_Cw	k_Rw
15	1	10.1805	1.18E+03	3.84E-09	4.79E-05	2.09E+04
16	2	104.3247	912.7932	4.21E-09	8.36E-06	1.20E+05
17	3	107.3062	915.3741	4.52E-09	9.02E-06	1.11E+05
18	4	108.269	952.4862	4.06E-09	9.49E-06	1.05E+05
19	5	96.0073	956.5231	3.93E-09	9.02E-06	1.11E+05
20	6	104.5431	1.00E+03	3.84E-09	7.50E-06	1.33E+05
21	7	105.3437	945.43	4.12E-09	8.84E-06	1.13E+05
22	8	100.6079	939.5331	4.10E-09	8.96E-06	1.12E+05
23	9	93.5184	925.4692	3.96E-09	9.59E-06	1.04E+05
24	10	89.6174	959.8366	3.86E-09	8.80E-06	1.14E+05
25	11	89.9441	942.5097	4.15E-09	9.50E-06	1.05E+05
26	12	75.0116	901.4998	4.23E-09	1.01E-05	9.86E+04
27	13	89.7918	911.684	4.08E-09	9.73E-06	1.03E+05
28	14	92.8548	875.3989	4.08E-09	1.10E-05	9.09E+04
29	15	87.91	883.4215	4.13E-09	1.04E-05	9.58E+04
30	16	86.4393	869.529	4.02E-09	1.08E-05	9.23E+04
31	17	87.4764	869.0139	3.99E-09	1.09E-05	9.21E+04
1	18	90.4363	820.9791	4.14E-09	1.21E-05	8.26E+04
2	19	87.6199	847.4245	4.26E-09	1.13E-05	8.87E+04
3	20	94.6597	880.65	4.10E-09	1.06E-05	9.47E+04
4	21	96.0889	866.9934	4.10E-09	1.08E-05	9.25E+04
5	22	88.7451	889.6126	4.01E-09	1.02E-05	9.83E+04
6	23	90.7633	914.2283	4.09E-09	1.01E-05	9.89E+04
7	24	96.3756	921.7489	4.09E-09	1.00E-05	1.00E+05
8	25	49.6769	948.3867	3.33E-09	9.76E-06	1.02E+05
9	26	92.3784	854.7524	4.13E-09	1.16E-05	8.64E+04
10	27	92.9362	850.9064	4.05E-09	1.18E-05	8.50E+04
11	28	93.0756	893.1137	4.07E-09	1.04E-05	9.59E+04

Table 5.2 displays an example of the parameter extraction results: data from Sensor No.3 in 7.5 mM of glucose solutions. With the extracted data, the potential correlation could be investigated.

5.3   Parameter Correlation Attempt

The parameter extraction is performed with the EIS measurement results for No. 0 sensor. Two types of graphs are plotted between each parameter with sensitivity m: both values versus time (in days) and the parameter versus the sensitivity.

5.3.1   Results from Sensor No. 0

Among all the graphs, two cases which seem to show some correlations between the parameters and the sensitivity will be discussed.

Figure 5.7: Sensor No. 0: Sensitivity m vs. double layer capacitance C_d

Figure 5.7 shows double-layer capacitance C_d and sensitivity vs. time (left) and C_d vs. m (right) at $20mM$ glucose concentration. C_d and m versus time displays an approximate inverse proportionality between these two parameters. Then C_d versus m shows two clear clusters of data which indicates different performances before/after the instant drop (at day 15).

According to the data acquired from the extraction, only rough relationship could be found: when the double-layer capacitance C_d is around 4 nF, the sensor is not yet degraded and its sensitivity is close to the value of $1 \times 10^{-6} A/M$. When C_d increases to 7 nF, it indicates that the sensitivity already drops to approximately half of its original value.
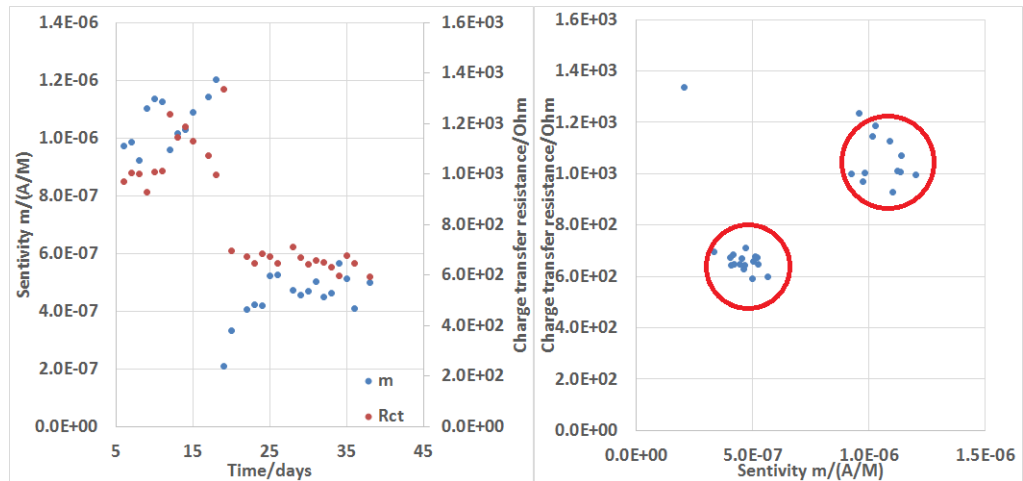
Figure 5.8: Sensor No. 0: sensitivity m vs. charge transfer resistance R_{ct}

The same kind of analysis is made with charge transfer resistance R_{ct} with sensitivity, as shown in Figure 5.8. Similarly, direct proportion relationship seems to exist between R_{ct} and m, which also shows two distinct clusters of data.

Similar relationship could be stated as: when the charge transfer resistance R_{ct} is around 1100 Ω, the sensor may work properly with m value of about $1 \times 10^{-6} A/M$. However, when R_{ct} drops to 700 Ω, it implies the sensitivity degradation has happened.
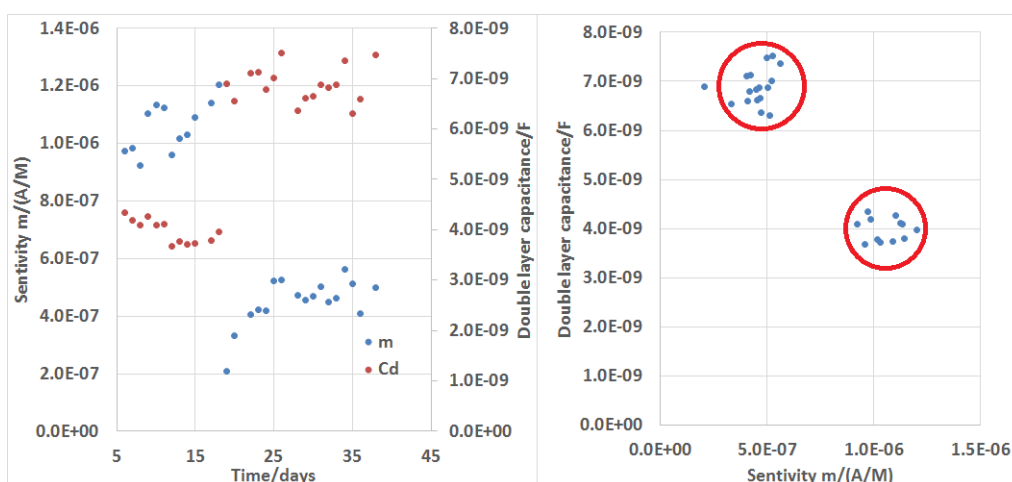
5.3.2   Results from Sensor No. 1 to 3
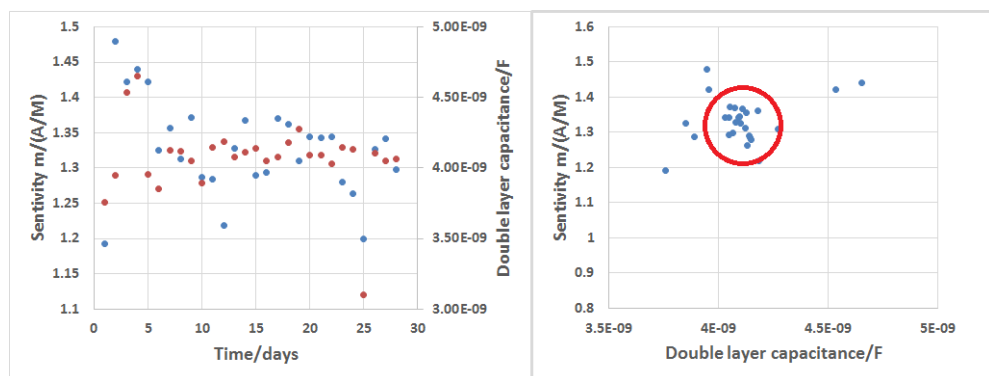
Figure 5.9: Sensor No. 3: Sensitivity m vs. double layer capacitance C_d

Figure 5.9 display the double-layer capacitance C_d and sensitivity vs. time (left) and C_d vs. m (right) at $2.5mM$ glucose concentration for sensor No.3 in the second set

of measurements. It is relatively clear that there is only one cluster of data points. The range of this cluster is generally the same as one of the clusters measured with sensor No. 0.

The cluster of data for sensor No. 3 is generally located the same position when sensor No. 0 is not degraded. This is consistent with the previously result.
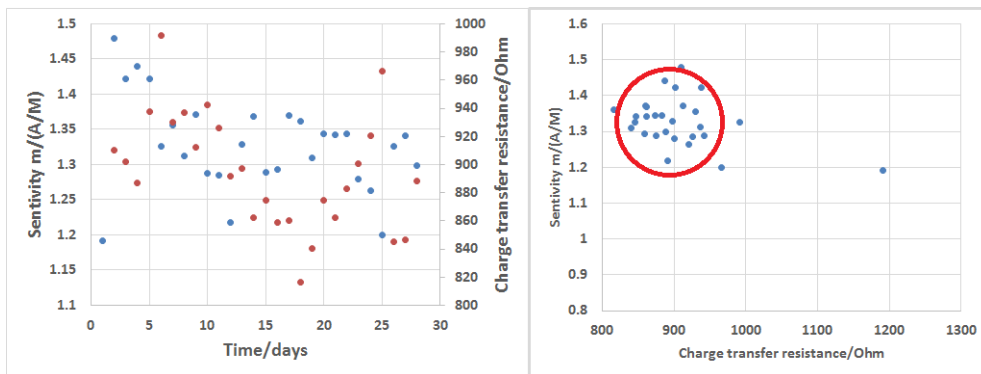
Figure 5.10: Sensor No. 3: Sensitivity m vs. double layer capacitance C_d

Similarly, the possible relationship between charge transfer resistance R_{ct} with sensitivity, as shown in Figure 5.10, is plotted. Besides the only one point at the right end which is apparently the outlier, the attribution of data points is still within one of the clusters measured with sensor No. 0.

The circle from this clustering of the data of sensor No.3 is located at generally the same position as the previous scattering plot (although with a larger radius). This indicates that this correlation might also be seen when m drops.
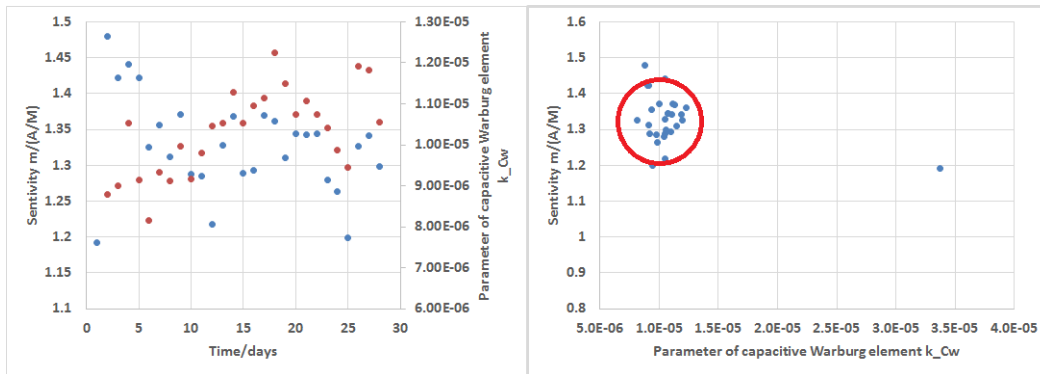
Figure 5.11: Sensor No. 3: Sensitivity m vs. parameter of capacitive Warburg element k_{C_w}

As mentioned in equation 3.3, the Warburg element can be divided in to a capacitive and a resistive elements in series. Since both the element is frequency dependent, k_{C_w} is the frequency-independent parameter which equal to $\frac{1}{\sigma}$.

Similarly to the previous graph, although there appears to be some relationship by observing these two values versus time. After plotting k_{C_w} vs. m, the relationship is actually relatively vague as only one cluster of data points is found.

Chapter 6

PCB Design

T HE general scheme of the whole system is shown in Figure 6.1. In this section, design of PCB (the left block) will be discussed. When executing option one, which is simple chronoamperometry measurement, wave generator only produces DC signal ($0.53V$) while option two of EIS will require both DC and AC signals from the generator and the result will be processed by a lock-in amplifier. Options selection and signal generation will be controlled by the micro-controller.
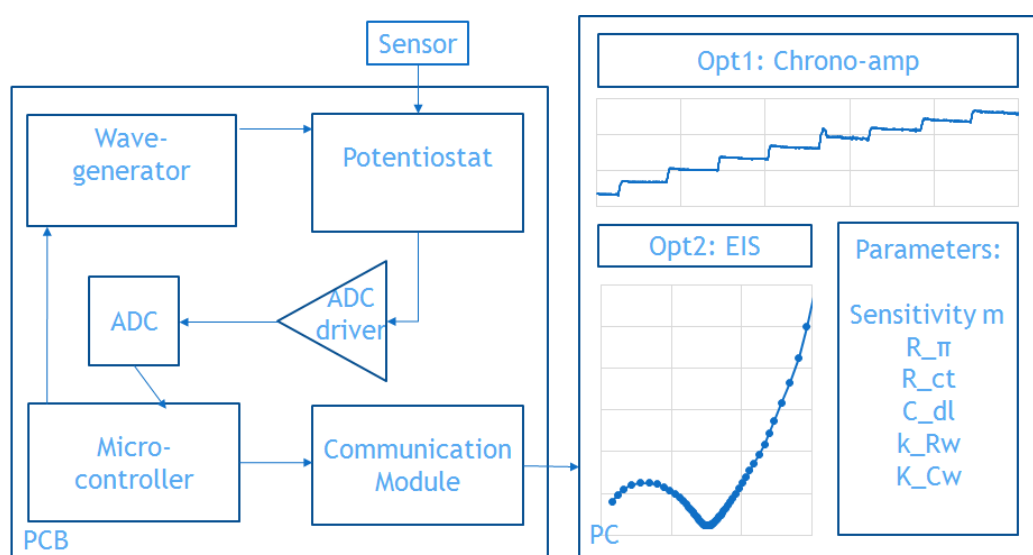
Figure 6.1: Block diagram of designed PCB with PC display.

6.1 Design of Potentiostat

The general scheme of potentiostat is shown in Figure 6.2. As mentioned in previous sections, the fundamental function of a potentiostat is to maintain the potential difference between RE and WE of the sensor in a steady value (as small fluctuations as possible). Value of the potential V_{cell} required is determined by the category of the targeted molecules (glucose in this case), its corresponding oxidase (GOx) and the specific model of the sensor circuitry. As stated in previous section, the value is $0.53V$.

The potentiostat is also designed to supply and deliver the current I_{cell}, which passes through (either from and into) WE-CE pair, to the read out-stage. WEs are all grounded in this section. This is a simple configuration to ensure the potential difference between RE and WE is fixed to be the input voltage level V_{in}. This function will be discussed in the next section.
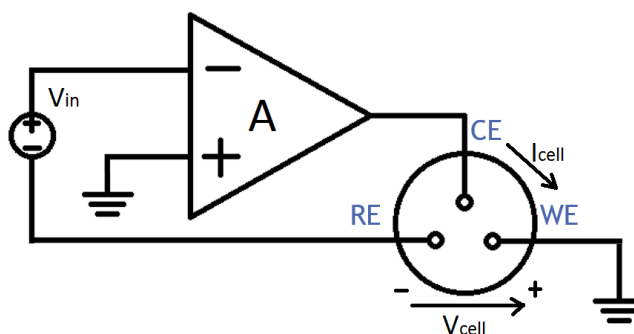
Figure 6.2: General Idea of potentiostat to keep the potential static.

This simple structure could almost accomplish the task. However, there is relatively high requirement on the input signals. Since neither ports of the input (-ve input of the amp and RE) is connected to the real ground, the wave generator is required be capable of generating required signals which should be differential and floating, of which the demand is hardly met by the mainstream function generators [2].

Meanwhile, the input signal would normally consist of many components, such as a constant offset (DC level), a ramp voltage and/or a sinusoidal signal (for spectroscopy) hence it is necessary to prepare multiple entries to the input port.

An improved version of the potentiostat is depicted in Figure 6.3. This structure solves the problem of floating input and also meets the multiple inputs requirement.
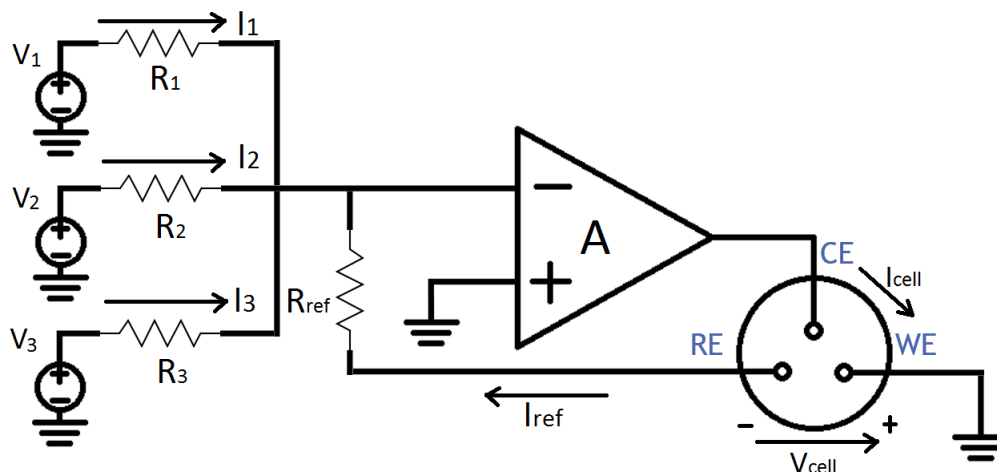
Figure 6.3: Basic scheme of potentiostat with multiple input signals.

According to Kirchhoff's Current Law, sum of the currents flowing through the assembly point on the negative input of the amplifier should be zero, which yields:

$$-I_{ref} = I_1 + I_2 + I_3 \tag{6.1}$$

It can also be expressed as:

$$-V_{ref} = V_1 \left(\frac{R_{ref}}{R_1} \right) + V_2 \left(\frac{R_{ref}}{R_2} \right) + V_3 \left(\frac{R_{ref}}{R_3} \right) \tag{6.2}$$

Typically, values of all resistors mentioned in equation 6.2 are identical, hence the sums of voltages from inputs can be transferred to RE:

$$-V_{ref} = V_1 + V_2 + V_3 \tag{6.3}$$

And the potential difference between WE and RE remains V_{ref}, which could be altered simply by changing the values of input resistors R_1, R_2 and R_3.

Nonetheless, this refined design also suffers from a major drawback that the RE might need to provided a excessive huge value of current [2]. A simple voltage follower is

added into the feedback loop as a buffer (shown in Figure 6.4).
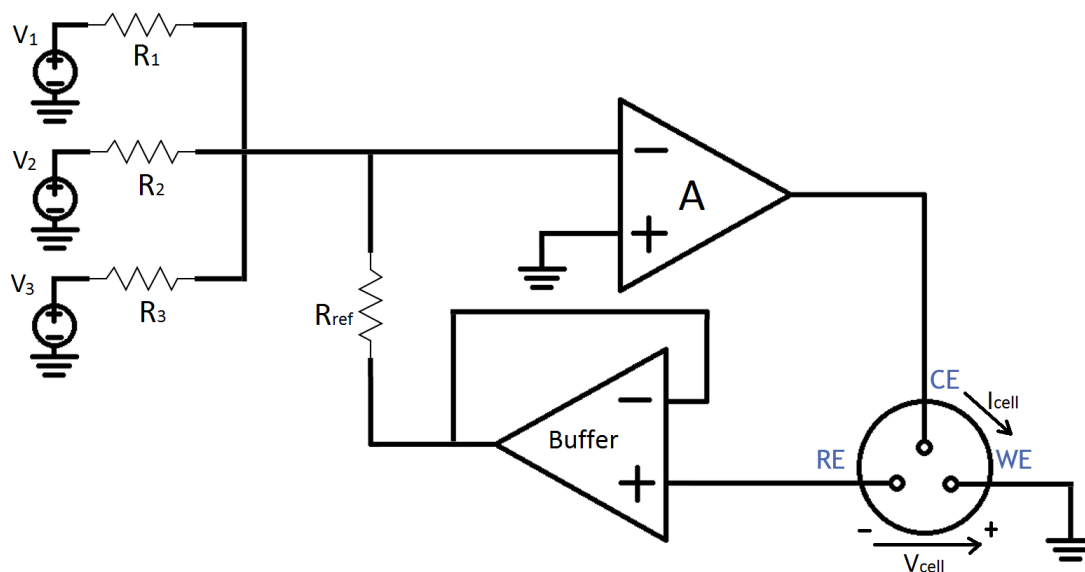
Figure 6.4: Potentiostat with a voltage-follower as the buffer.

As indicated in Figure 6.4, the buffer with massive input impedance reduces the current load on RE, I_{ref} while maintain the required potential.

It is worth noting that the open loop gain of the buffer amplifier should be large enough to be used as a voltage follower, which passes the exact potential from the input (RE) to the output.

Moreover, the original upper amplifier is required to have significantly small input bias current, as well as huge input impedance [12]. The former one could be optimised by selecting a suitable op-amp model while the latter problem can be solved by simply adding another voltage buffer before the input.

6.2 Design of Current Read-out Stage

The potentiostat is also designed to supply the current I_{cell}, which is essential for the desired reactions in the solution. It also could feed this current value, to the next stage, read-out stage.

Several circuit configurations are available to realise this functionality, but can classified into two categories: grounding WE or grounding CE, of which the former is more prevalent [12]. Essentially, these two methods both works as a current-voltage converter and the gain is both the corresponding resistor in the designs.

Figure 6.5 depicted a commonly-used structure for current read-out with WE grounded.
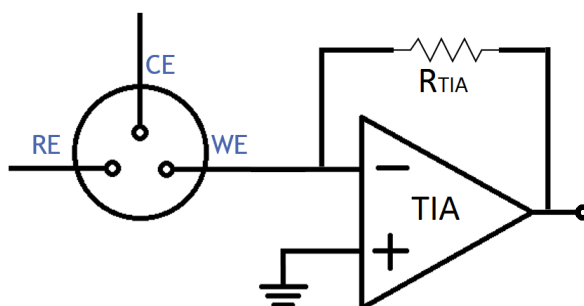
Figure 6.5: A transimpedance amplifier readout stage.

In this configuration, current from CE to WE, through the electrochemical cell, is fed into a transimpedance amplifier (TIA) with a resistor, R_{TIA}. Output of the configuration is converted from current into voltage signal. It can be deduced that the transimpedance gain is exact the value of the resistor, $A_Z = R_{TIA}$. This configuration can also be regarded as a current follower, of which the output follows the input to a certain degree of amplification.

The advantage of this structure is that it still keeps the WE to the ground (virtual ground actually), which maintain the crucial potential difference of the whole measurement system.

One of the points to be noted is the noise in this stage. It can be separated by adding a suitable capacitor in parallel with the resistor, which constitutes a simple filter. Moreover, the input impedance of the amplifier should be huge enough to reduce the input offset current, in order to reduce the read-out error.

Another possible and popular configuration is also based on the grounded WE. As shown in Figure 6.6, an instrumentation amplifier is adopted here to measure the voltage
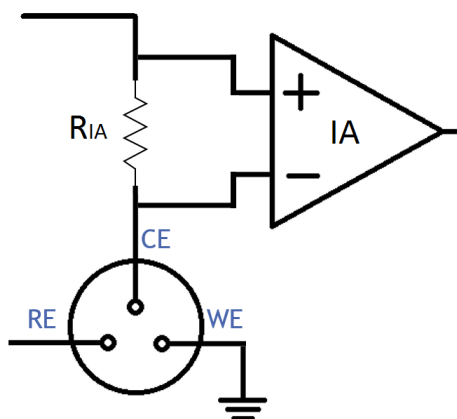
Figure 6.6: An instrumentation amplifier readout stage.

difference on both ends of a specified value of resistance on the CE.

The targeted current value is now measured on CE instead of WE, which means WE is still directly connect to the real ground. This kind of configuration is thought to be more accurate , as the potential difference V_{cell} is more stable than the previous one, with WE virtual-grounded.

To make the configuration feasible, an assumption is made that the current passing the resistor, R_{IA}, is identical to the desired current flowing through the cell [12].

6.3   Design of EIS Configuration

One of the major differences of impedance measurement from chronoamperometry is the input signal. EIS normally requires a sinusoidal wave with relatively small amplitude ($5mV$ in this design) added to the input terminal of the potentiostat. Frequency of ac signal would then change from 10 to $1MHz$ as the measurement conducted in lab.

EIS measurement could be conducted by two possible means, data are either measured in frequency domain directly with one kind of instrument called frequency response analyzer, or in time domain then transferred into frequency domain with Fourier transformation (generally DFT) [2].

The basic principle in this configuration is similar to a demodulator in telecom-
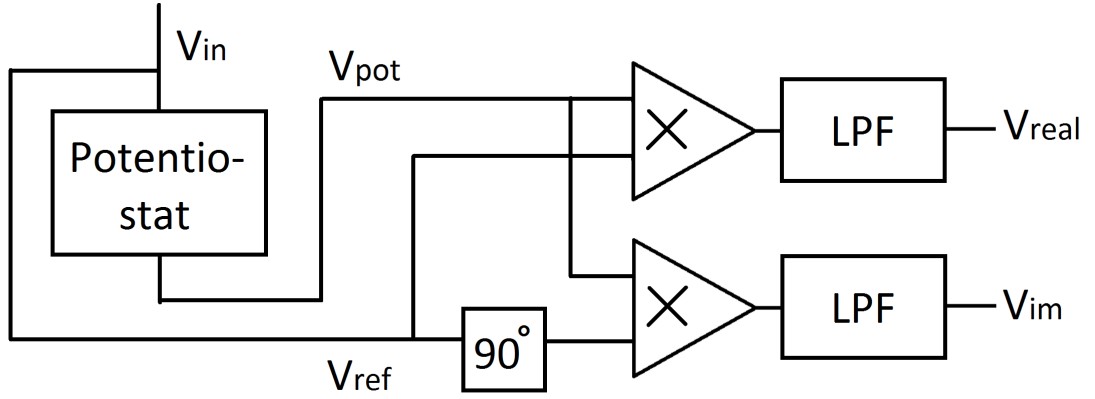
Figure 6.7: **General scheme of a lock-in stage for the calculation of real/imaginary parts.**

munication applications, signals are partially phase-shifted and mixed with the original signal, the product is then filtered by some LPFs to separate the targeted components (shown in Figure 6.7).

V_{pot} stands for the output of the potentiostat stage which can be expressed as:

$$V_{pot}(t) = V_{OUT}sin(2\pi ft + \Phi_{pot}) \tag{6.4}$$

while V_{ref} represents the input signal of the potentiostat stage, as a reference signal for the mixer:

$$V_{ref}(t) = V_{IN}sin(2\pi ft) \tag{6.5}$$

Therefore, the results of two prallel mixers can be calculated:

$$V_{Re.raw} = V_{OUT}sin(2\pi ft+\Phi_{pot}){\cdot}V_{IN}sin(2\pi ft) = \frac{1}{2}V_{IN}V_{OUT}\left(cos(\Phi_{pot}) - cos(4\pi ft + \Phi_{pot})\right) \tag{6.6}$$

$$V_{Im.raw} = V_{OUT}sin(2\pi ft+\Phi_{pot}){\cdot}V_{IN}cos(2\pi ft) = \frac{1}{2}V_{IN}V_{OUT}\left(sin(\Phi_{pot}) + sin(4\pi ft + \Phi_{pot})\right) \tag{6.7}$$

After the mixers, both real and imaginary voltage signals should be filtered as the targeted components are only the DC parts.

$$V_{Re} = \frac{1}{2} V_{IN} V_{OUT} cos(\Phi_{pot}) \tag{6.8}$$

$$V_{Im} = \frac{1}{2} V_{IN} V_{OUT} sin(\Phi_{pot}) \tag{6.9}$$

Since the output from the potntiostat can be represented by the cell current:

$$V_{pot} = I_{cell} R_{gain} \tag{6.10}$$

As a result, the desired impedance and phase of the unknown electrochemical cell can be represented as:

$$|Z_{cell}| = \frac{V_{IN} V_{cell} R_{gain}}{2 \cdot \sqrt{V_{Re}^2 + V_{Im}^2}} \tag{6.11}$$

$$\Phi_{cell} = arctan\left(\frac{V_{Im}}{V_{Re}}\right) \tag{6.12}$$

It is worth noting that this part is finally realised in digital, which requires less resources than implementation of analogue mixers and following filters.

6.4   PCB Schematic

The whole system consists of three main blocks: a) A measuring module (marked with blue in Figure 6.8) that supplies configurable signal (both AC and DC) in to the potentiostat which controls the constant potential between WE and RE; b) A digitisation module (marked with red in Figure 6.8) that receives the supply signal as well as the output signal from potentiostat and transfer it to a differential one to be digitised by an ADC; c) An external micro-controller (not included in the PCB) which controls the input of the wave generator and processes the output of the ADC in the form of Bode and Nyquist plots with the desired parameters.

The first module, which mainly consists of a wave generator, a potentiostat and a signal readout stage. AD9833 (Analog Devices), a low power, programmable waveform generator is used to supply a DC offset with a sinusoidal signal of which the frequency
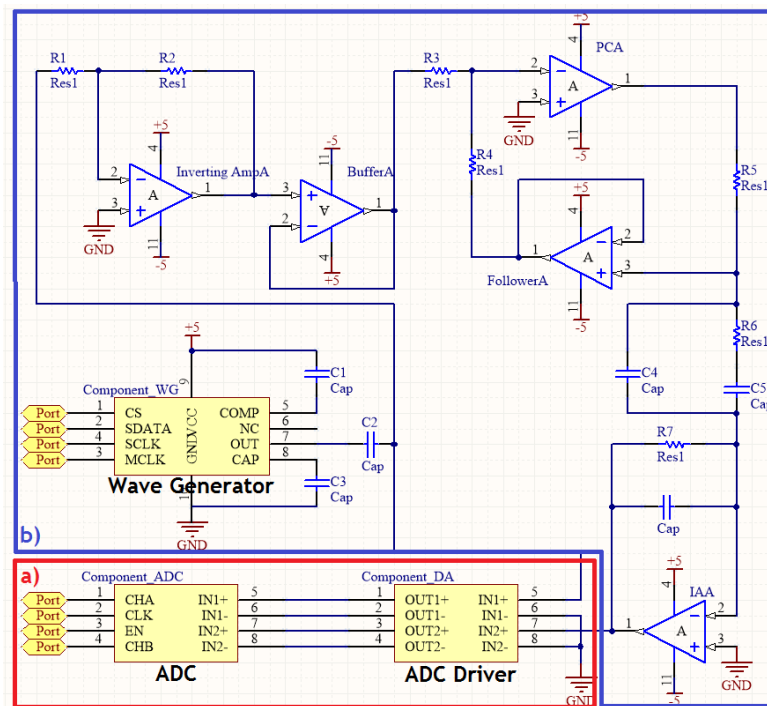
Figure 6.8: Schematic of the system in Altium Designer

is configurable in a wide range, from 0 to 12.5 MHz. The generator is controlled by the micro-controller which would be mentioned later.

Signal generated is fed into a potentiostat stage, which includes an inverting amplifier, a buffer, a potential-control amplifier and a voltage follower (in the feedback loop). A model of high-speed JFET amplifier from Analog Devices, ADA4610 is employed for these four places. ADA4610 features very low input noise voltage, current noise, offset voltage and input bias current.

The current readout stage is simply a transimpedance amplifier (TIA) with certain value of impedance in its feedback loop. Another approach is to use an instrumentation amplifier to transfer the current signal to a voltage one. AD8421 from Analog Device with relatively low bias current and noise is employed here. The (transimpedance) gain of this stage is simply the value of impedance here.

The second module, digitisation module is based on an ADC driver and an ADC. Since the output from the current readout stage is a single ended signal hence before its

connection with the ADC, a driver, AD8138, to convert it to a differential one is necessary. A National Semiconductor ADC, ADC12D040, is employed after the driver to digitised the input differential signal into 12-bits words, at high speed.

The last module, the micro-controller is generally responsible for the signal processing. The function of calculating the real and imaginary parts of the impedance was originally assigned to either an ADuCM350 or an AD5933 chip, which are both capable of the job. However, neither of their working frequency ranges covers the required 1 to 1M Hz. Therefore, the direct method of calculating it inside the controller is employed. The functionality of a lock-in amplifier (mentioned in the previous section) is performed on a National Instruments platform, SBRI09632, to realised the real-time calculation of the magnitude and phase simultaneously.

The chips selected are concluded in the following table.

Table 6.1: Selected components for PCB implementation

Module	Device Name	Model No.	Manufacturer
Measuring	Operational Amp	ADA4610	Analog Devices
	Instrumentation Amp	AD8421	Analog Devices
Digitisation	ADC Driver	AD8138	Analog Devices
	ADC (selection1)	ADC12D040	Texas Instruments
	ADC (selection2)	AD7357	Analog Devices
ucontroller	microcontroller	SBRIO9632	National Instruments

Chapter 7

Conclusion

7.1 Discussion

I N this chapter, reflections on the restrictions which might influence the accuracy of the measurements are presented. Afterwards, some possible research directions in association with this measurements would be discussed. After the discussion, the thesis would be concluded.

7.1.1 Limitations of the Study

First of all, the noise affect could not be ignored. There were other electronic devices in the same laboratory besides the CH Instruments Electrochemical Station, which could cause certain levels of noise (different devices might be on for different day's measurements). Meanwhile, the soldering spots of the cable which connected the Station with the sensor were exposed hence these spots could be where the noise signal came into the measuring configuration.

It is worth noting that in the first set of measurements, a magnetic stirrer was employed inside the solution to keep it dynamic (maintain the uniformity of the solution) which would also bring in some noise. When in the second set of measurements, no the magnetic stirrer was used hence no such noise was introduced. However, the solution might not be suitable for measurement in that case (the solvent was not uniformly distributed)

which introduced another uncertainty in the measurement results.

As a result, a relatively optimised method is to introduce a Faraday Cage to isolate the entire measurement configuration. Meanwhile, a magnetic stirrer should be used to keep the solution dynamic to ensure a better accuracy in measurement. Besides these actions, the soldering spots should be covered to avoid more noise.

The second part of the discussion is on the theoretical model of the sensor's equivalent circuit, the Randles model (shown in Figure 3.1) which is actually a simplified model which considers the interface of electrode and electrolyte as a pure capacitor C_{dl}. This element in reality, named constant phase element (CPE), is frequency dependent and functions similar to a capacitor. As a matter of fact, this kind of constant phase phenomenon happens when there is an interface consisting of metal, insulator and solution [37] [38] [39].

The mathematical expression of a CPE can be represented as:

$$Z_{CPE} = \frac{1}{Y_{C0}(j\omega)^n}$$ (7.1)

where Y_{C0} is the admittance of a pure capacitance (which is the simplified double layer capacitor) and n, a fractional exponent is a CPE constant, with value range from 0 to 1 [40]. It is worth noting that when $n = 1$, CPE works like an ideal capacitor and when $n = 0$, it behaviours like an ideal resistor.

As a result, the simplification of CPE can be another source of inaccuracy in measurement/extraction.

7.1.2 Future Research

One potential research direction focuses on the temperature of the experimental environment as it affect the solubility of both PBS and glucose. It would be necessary to control the solution temperature constant for each measurements by letting it stand for the same amount of time after taken out from the refrigerator.

Another direction would pay attention to the storage solution. In this thesis, both $20.0mM$ and $5.0mM$ of glucose solution (solved in $100mM$ PBS solution in distilled water)

were employed. However, glucose level in human blood actually changed dramatically over a day, such as before/after meals. Therefore, the concentration of glucose for storage solution is also worth another look.

And there is also a potential way to study the sensitivity a glucose sensor even the drop is still not observed. The values of residuals in sensitivity m versus time can be investigated to see whether there is a potential trend.

Moreover, the structure of current used sensor includes a membrane, which could possibly effect the performance of sensitivity. Therefore, by using a sensor without membrane could be another chioce to study the sensitivity degradation.

Last but not least, since the commercialised model of glucose sensor is through huge amount of research and development, it is highly likely that the sensor could be capable of more than 14 days of extended use. Therefore, the measurements would go on until the drop in sensitivity is observed.

7.2   Conclusion

The purpose of the thesis is to study the impedance of the sensor over time in an attempt to develop a new algorithm to predict the sensor performance. In particular this research studies the correlation of the impedance with sensor sensitivity over time. The thesis mainly describes the experimental setup, method and results of the chronoamperometry and EIS measurements of Enlite$^{\text{TM}}$ glucose sensors as well as some reflections on the whole process.

The sensitivity and the impedance of the sensors were measured over time, one sensor for 45 days and the other three for 35 days. Sensitivity m of sensor appears to be correlated with double-layer capacitance Cd (inverse proportionality) as well as the charge-transfer resistance Rct (direct proportionality) for first set of measurement results. To confirm this, three similar sensors are under measurements. Until Day 45 of measurement, still no drop in sensitivity is observed.

Till now, it is still not clear that whether the correlation found in the first sensor

was an outlier or not. Since no similar sensitivity drop is observed in the current 3 sensors, this implies that the abrupt drop happened to sensor No. 0 in the first set of measurement could be an outlier. Nevertheless, the measurements are still ongoing until the sensitivity drop is observed, when the EIS results may clarify the correlations found for the first sensor.

References

[1] A. T. Da-Poian, T. El-Bacha, and M. R. M. P. Luz, "Nutrient utilization in humans: Metabolism pathways," *Nature Education*, vol. 3, no. 9, p. 11, 2010.

[2] A. Bard and L. Faulkner, Eds., *Electrochemical Methods, Fundamentals and Applications.* John Wiley and sons inc., 2001.

[3] S. Carrara, A. Cavallini, V. Erokhin, and G. D. Micheli, "Multi-panel drugs detection in human serum for personalized therapy," *Biosensors and Bioelectronics*, vol. 26, no. 9, pp. 3914–3919, 2011.

[4] C. Lamanna, "Studies of endogenous metabolism in bacteriology," *Annals of the New York Academy of Sciences*, vol. 102, no. 3, 1963.

[5] G. D. Micheli, S. Ghoreishizadeh, C. Boero, F. Valgimigli, and S. Carrara, "An integrated platform for advanced diagnostics," in *Design, Automation and Test in Europe (DATE)*, March 2011, p. 16.

[6] H. Bisswanger, Ed., *Enzyme Kinetics: Principle and Methods.* Wiley, 2002.

[7] D. L. Purich, Ed., *Enzyme Kinetics: Catalysis and Control.* Elsevier, 2010.

[8] R. A. Copeland, Ed., *Enzymes: A Practical Introduction to Structure, Mechanism, Data Analysis, 2nd ed.* Wiley, 2000.

[9] Q. H. Gibson, B. E. P. Swoboda, and V. Massey, "Kinetics and mechanism of action of glucose oxidase," *The Journal of Biological Chemistry*, vol. 239, pp. 3927–3934, 1964.

[10] M. C. Tsai and Y. C. Tsai, "Adsorption of glucose oxidase at platinummultiwalled carbon nanotube-alumina-coated silica nanocomposite for amperometric glucose biosensor," *Sensors and Actuators B: Chemical*, vol. 141, no. 2, pp. 592–598, 2009.

[11] S. Schumacher and et al., "Highly-integrated lab-on-a-chip system for point-of-care multiparameter analysis," *Lab on a Chip*, vol. 12, no. 3, pp. 464–473, 2012.

[12] T. Rinken, Ed., *State of the Art in Biosensors - General Aspects.* InTech, March 2013.

[13] E. A. H. Hall, Ed., *Biosensors.* Open University Press, 2000.

[14] B. Pejcic and R. D. Marco, "Impedance spectroscopy: Over 35 years of electrochemical sensor optimization," *Electrochimica Acta*, vol. 51, pp. 6217–6229, 2006.

[15] A. Gill, G. Farace, G. Lillie, and P. Vadgama, "Strategic issues in reliable sensing," *Bioelectrochemistry*, vol. 55, pp. 123–125, 2002.

[16] M. Koudelka-Hep and P. D. van der Wal, "Microelectrode sensors for biomedical and environment applications," *Electrochimica Acta*, vol. 45, pp. 2437–2441, 2000.

[17] J. Wang, Ed., *Analytical Electrochemistry 2nd ed.* Wiley/VCH, 2000.

[18] A. Barton and et al., "Sonochemically fabricated microelectrode arrays for biosensors offering widespread applicability: Part i," *Biosensors and Bioelectronics*, vol. 19, p. 328, 2004.

[19] S. X. Zhang and et al., "Covalent attachment of glucose oxidase to an au electrode modified with gold nanoparticles for use as glucose biosensor," *Bioelectrochemistry*, vol. 67, no. 1, pp. 15–22, 2005.

[20] S. M. Martin, F. H. Gebara, T. D. Strong, and R. B. Brown, "A fully differential potentiostat," *IEEE Sensors Journal*, vol. 9, no. 2, pp. 135–142, 2009.

[21] M. M. Ahmadi and G. A. Jullien, "Current-mirror-based potentiostats for three-electrode amperometric electrochemical sensors," *IEEE Transactions on Circuits and Systems*, vol. 56, no. 7, pp. 1339–1348, 2009.

[22] J. E. B. Randles, "Kinetics of rapid electrode reactions," *Discussions of the Faraday Society*, vol. 1, no. 11, 1947.

[23] D. E. Smith, *Critical Reviews in Analytical Chemistry*, vol. 1, no. 1, 1966.

[24] N. Fouquet, "Real time model-based monitoring of a pem fuel cell flooding and drying out," *Vehicle Power and Propulsion Conference (VPPC), IEEE*, pp. 1–8, 2010.

[25] M. Sluyters-Rehbach and J. H. Sluyters, *Journal of Electroanalytical Chemistry*, vol. 4, no. 1, 1970.

[26] B. E. Conway, Ed., *Electrochemical Capacitor, Scientific, Fundamentals and Technological Applications.* Plenum Press, 1999.

[27] J. R. Scully, D. C. Silverman, and M. W. Kendig, Eds., *Electrochemical Impedance: Analysis and Interpretation.* ASTM Special Technical Publication, 1993.

[28] E. Barsoukov and J. R. Macdonald, Eds., *Impedance Spectroscopy: Theory, Experiment, and Applications.* Wiley, 2005.

[29] N. C. Martin and et al., "Phenobarbitone-induced ploidy changes in liver occur independently of p53," *Toxicology Letters*, vol. 119, pp. 109–115, 2001.

[30] N. Martin and et al., "Functional analysis of mouse hepatocytes differingin dna content: Volume, receptor expression,and effect of ifnγ," *Journal of Cellular Physiology*, vol. 191, pp. 138–144, 2002.

[31] D. P. K. Ng and et al., "Effect of storage conditions on the extraction of pcr-quality genomic dna from saliva," *Clinica Chimica Acta*, vol. 343, pp. 191–194, 2004.

[32] R. Dulbecco and et al., "Plaque formation and isolation of pure lines with poliomyelitis viruses," *The Journal of Experimental Medicine*, vol. 99, no. 2, pp. 167–182, 1954.

[33] M. Berman, "Large sample bias in least squares estimators of a circular arc center and its radius," *CVGIP: Image Understanding*, vol. 45, pp. 126–128, 1989.

[34] V. Pratt, "Direct least-squares fitting of algebraic surfaces," *Computer Graphics*, vol. 21, pp. 145–152, 1987.

[35] A. Al-Sharadqah and N. Chernov, "Error analysis for circle fitting algorithms," *Electronic Journal of Statistics*, vol. 3, pp. 886–911, 2009.

[36] G. Taubin, "Estimation of planar curves, surfaces and nonplanar space curves defined by implicit equations, with applications to edge and range image segmentation," *IEEE Trans. Pattern Analysis Machine Intelligence*, vol. 13, pp. 1115–1138, 1991.

[37] M. Itagaki, A. Taya, K. Watanabe, , and K. Noda, "Deviation of capacitive and inductive loops in the electrochemical impedance of a dissolving iron electrode," *The Japan Society for Analytical Chemistry*, vol. 18, pp. 641–644, 2002.

[38] J. R. Macdonald, Ed., *Impedance Spectroscopy Emphasizing Solid Materials and Systems*. New York: Wiley, 1987.

[39] P. Zoltowski, "On the electrical capacitance of interfaces exhibiting constant phase element behavior," *Journal of Electroanalytical Chemistry*, vol. 443, pp. 149–154, 1998.

[40] J. Bisquert and et al., "Doubling exponent models for the analysis of porous film electrodes by impedance: Relaxation of tio nanoporous in aqueous solution," *The Journal of Physical Chemistry*, vol. 104, pp. 2287–2298, 2000.

Appendix A

Code for parameter extraction

```matlab
1  results = zeros(18,6);
2  n = 1;
3  for n = 1:18
4
5  a = xlsread('\\icnas3.cc.ic.ac.uk\xz15\Desktop\EISdata\Aug\11-08.xlsx',n);
6  x0 = a(11:30, 2);                                    %range of data for
       circle fitting
7  y0 = -a(11:30, 3);
8  Par = CircleFitByTaubin([x0 y0]);
9  drawcircle(Par(1,1), Par(1,2), Par(1,3));
10 plot (a(:, 2), -a(:, 3), 'o', 'MarkerSize',3);
11 grid on;
12 hold on;
13
14 Rpi = Par(1,1) - ((Par(1,3))^2-(Par(1,2))^2)^0.5;
15 Rct = 2 * ((Par(1,3))^2-(Par(1,2))^2)^0.5;
16
17
18 xpeak = Par(1,1);                                    %peak of semi-circle
19 ypeak = Par(1,2) + Par(1,3);                         %peak of semi-circle
20
21 for i = 11:30                                        %Method 1
22     if (a(i, 2) < xpeak)
23         n = i;
24     else
25         if abs(a(i, 2) - xpeak) >= abs(xpeak - a(i-1, 2))
```

```matlab
26              n = i − 1;
27          else
28              n = i;
29          end
30          break
31      end
32 end
33 fo1 = a(n, 1);
34
35
36 x2 = a(11:30, 1);                          %Method 2
37 y2 = log10(a(11:30, 2));                   %linear fitting log(
      Zreal) vs freq
38 coeffs2 = LinearRegression( x2, y2 );
39 fo2 = (log10(xpeak) − coeffs2(1))/coeffs2(2);
40
41
42 x3 = log10(a(11:30, 1));                   %Method 3
43 y3 = −a(11:30, 3);                         %polynomial fitting Zimg
       vs log(freq)
44 coeffs3 = polyfit( x3, y3, 2 );
45 syms x;
46 fun = coeffs3(1) ∗ x^2 + coeffs3(2) ∗ x^1 + coeffs3(3) ∗ x^0;
47 difffun = diff ( fun, x );
48 fo3 = 10^((−coeffs3(2)+(coeffs3(2)^2−4∗coeffs3(1)∗(coeffs3(3)−ypeak))^0.5)
      /(2∗coeffs3(1)));
49
50
51
52 fo = (fo1 + fo2 + fo3)/3;
53 Cd = 1/(fo2 ∗ Rct);                        %OR NEED TO BE DEVIDED
      BY 2∗pi
54
55
56
57
58 coordX = a(45:51, 2);                      %range of data for
      linear regression
59 coordY = −a(45:51, 3);
```

```matlab
60  coeffs = LinearRegression( coordX, coordY );
61
62  xlinear = xpeak:1:5000;
63  ylinear = coeffs(1) + coeffs(2)* xlinear;
64  plot(xlinear, ylinear, 'g');
65  hold on;
66
67  ZRE = - coeffs(1)/coeffs(2);
68  sigma = ((Rpi+Rct-ZRE)/(2*Cd))^0.5;
69  k_Cw = sigma^-1;                                %multiplied by w^(-1/2)
70  k_Rw = sigma;                                   %multiplied by w^(-1/2)
71
72
73  results(n,1) = n;
74  results(n,2) = Rpi;
75  results(n,3) = Rct;
76  results(n,4) = Cd;
77  results(n,5) = k_Cw;
78  results(n,6) = k_Rw;
79
80  end
```

Appendix B

Experimental Setup Details
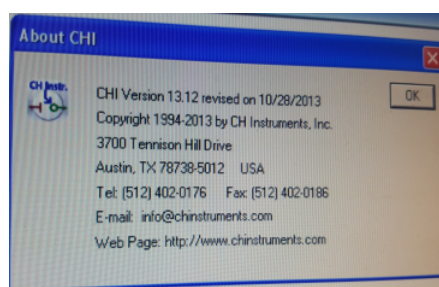
Figure B.1: **Software details working with CHI760E Electrochemical Workstation**
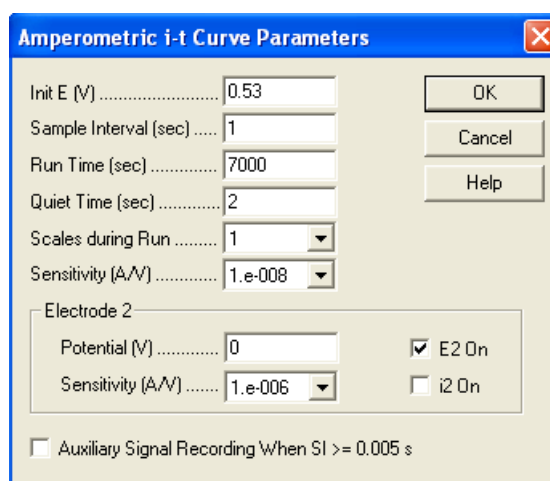
Figure B.2: **Settings for the function Amperometric i-t Curve**

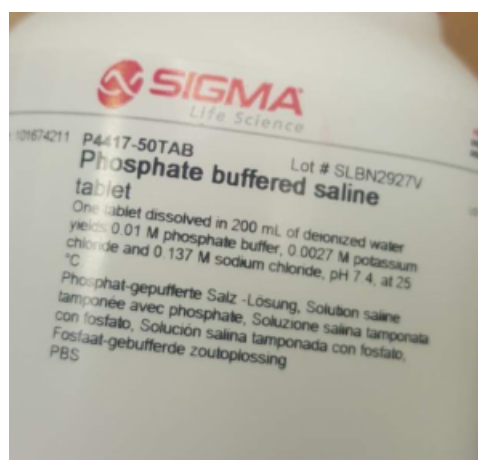**Figure B.3: Settings for the function A.C. Impedance**

Figure B.4: Phosphate Buffered Saline (PBS) tablets produced by Sigma Aldrich
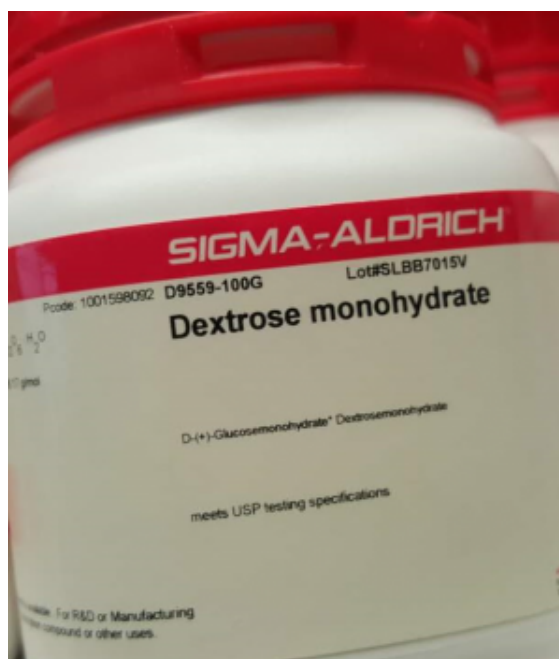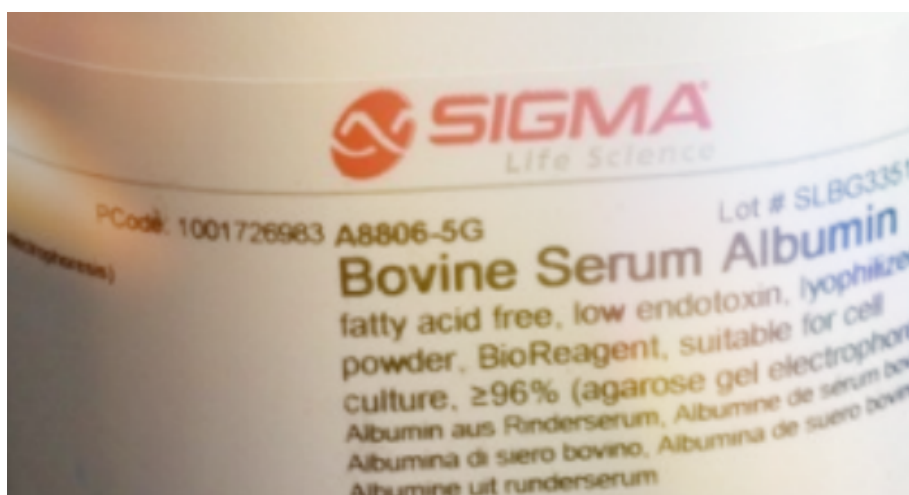
Figure B.5: Dextrose Monohydrate powder produced by Sigma Aldrich

Figure B.6: Bovine Serum Albumin powder produced by Sigma Aldrich